Chapter 11
Microstructure Aspects of the Deformation Mechanisms in Metastable Austenitic Steels

David Rafaja, Christiane Ullrich, Mykhaylo Motylenko and Stefan Martin

Abstract This chapter presents microstructure features, which are responsible for transformation-induced and twinning-induced plasticity in austenitic steels, gives an overview of relevant microstructure defects and shows how the microstructure defects and their interactions affect the deformation behaviour of these steels. Numerous examples illustrate the capability of scanning and transmission electron microscopy and X-ray and electron diffraction to detect, to identify and to quantify dislocations, stacking faults, twins and their clusters. In this context, the benefits of the in situ techniques of microstructure analysis are emphasized. As the presence and arrangement of stacking faults in austenite play a central role in the plasticity of the austenitic steels, a large part of this chapter is devoted to the characterization and description of their formation, widening and ordering. A novel method for determination of the stacking fault energy is presented that utilizes in situ X-ray or synchrotron diffraction under deformation. Finally, the dependence of the stacking fault energy on the chemical composition of the steel and on the deformation temperature is addressed, and considered as an effective tool for design of steels with desirable mechanical properties.

11.1 Introduction

The highly tunable properties of metastable austenitic steels are typically based on polymorphic phase transformations that allow a desired phase composition and microstructure of the steels to be adjusted. Moreover, the phase transformations and the twinning in metastable austenite are the most important mechanisms behind the transformation-induced plasticity (TRIP) and for the twinning-induced plasticity (TWIP) of these steels.

D. Rafaja (✉) · C. Ullrich · M. Motylenko · S. Martin
Institute of Materials Science, Technische Universität Bergakademie Freiberg,
Gustav-Zeuner-Straße 5, 09599 Freiberg, Germany
e-mail: rafaja@ww.tu-freiberg.de

At room temperature and ambient pressure, pure iron possesses *bcc* lattice that is stabilized by the ferromagnetic ordering of magnetic moments [1]. When the ferromagnetism is deactivated, e.g., through a high hydrostatic pressure (> 13 GPa), a hexagonal close packed modification of iron with a smaller specific volume becomes stable [2, 3]. Above 911 °C the *fcc* modification and above 1392 °C up to the melting point at 1536 °C the *bcc* structure are thermodynamically stable. By alloying iron with substitutional elements like chromium, nickel and manganese or with interstitial elements like carbon or nitrogen, the high temperature *fcc* phase can be stabilized down to room temperature. Such steels are known as *austenitic stainless steels*, as a high chromium content (> 12 wt%) impedes corrosion.

The *fcc* metals and alloys are usually ductile and show an excellent formability. Their stress-strain curves are characterized by the occurrence of high elongation and modest strain hardening that typically depend on the deformation temperature. In Fig. 11.1a, b, the temperature dependence of the mechanical behavior is illustrated on the true stress-strain curves measured under tensile load and on the strain hardening calculated from these stress-strain curves, respectively. The different characteristics of oxygen-free high conductive (OFHC) copper and a metastable austenitic stainless steel of the type X3CrMnNi16-6-6[1] illustrate the effect of the alloying elements. The yield stress and the applied stress needed to maintain plastic deformation are much higher for the alloyed steel than for the OFHC copper. Consequently, the alloyed steel shows a higher strain hardening than the OFHC copper.

Further differences are visible in the temperature dependence of the mechanical properties. Whereas the strain hardening of the OFHC copper increases only slightly
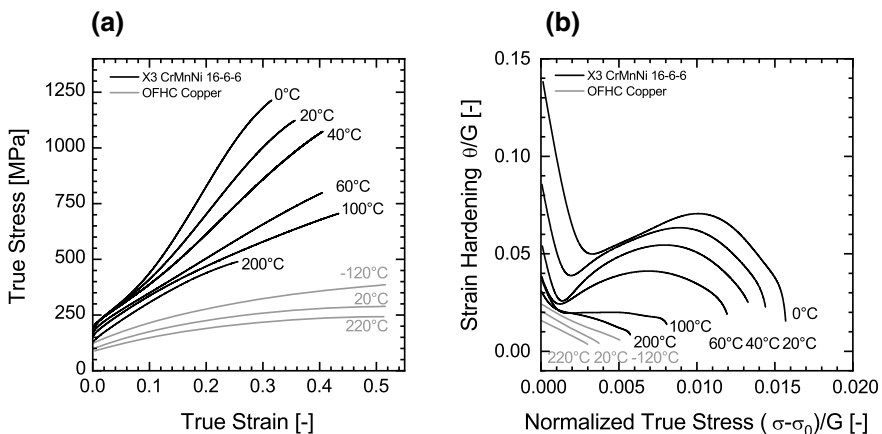

Fig. 11.1 Mechanical properties of X3 CrMnNi16-6-6 TRIP/TWIP steel [4] and pure (OFHC) copper [5] obtained from tensile testing at different temperatures: **a** stress-strain behavior and **b** corresponding strain hardening depicted in form of the Kocks-Mecking plot

---

[1]Chemical composition 16 wt% Cr, 6 wt% Mn, 6 wt% Ni, 1 wt% Si, 0.03 wt% C of the reference stainless steel in this Chapter, deviating chemical compositions from this one are given.

with decreasing deformation temperature, the increase of the strain hardening in the metastable austenitic steel plastically deformed at low temperatures is much more pronounced. Below 100 °C, the steel shows a tremendous increase of the strength and an additional hardening in the strain range between approx. 0.05 and 0.25. This difference in the temperature dependence of the mechanical properties can be explained by different deformation mechanisms in the OFHC copper and in the TRIP/TWIP steels, and by different activities of underlying microstructure defects and microstructure phenomena like dislocations, stacking faults and deformation-induced martensitic phase transformations.

In this Chapter, the role of dislocation slip, dissociation of dislocations, formation of partial dislocations, expansion of stacking faults and martensitic transformations in the plastic deformation of the TRIP/TWIP steels is discussed in order to explain the specific stress-strain behavior of these materials. Particular attention is paid to the effect of the stacking fault energy on the dislocation glide, nucleation of the martensites and to the interaction of microstructure defects and features among each other.

11.2 Fundamental Microstructure Defects, Their Activity and Configurations in Austenitic Steels

11.2.1 Dislocations and Stacking Faults in fcc Materials

Plastic deformation of metals is typically based on dislocation slip. Perfect dislocations in *fcc* austenite have the Burgers vectors ⟨110⟩ and glide on the close-packed planes {111}. In austenitic steels, the perfect dislocations tend to split into Shockley partial dislocations, which can be described by the following reaction:

$$\frac{a}{2}\left[10\bar{1}\right] \rightarrow \frac{a}{6}\left[11\bar{2}\right] + \frac{a}{6}\left[2\bar{1}\bar{1}\right] \tag{11.1}$$
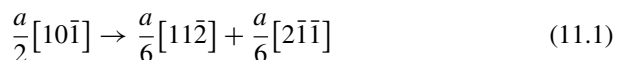
In (11.1), a is the lattice parameter of the *fcc* structure and $\frac{a}{2}\left[10\bar{1}\right]$ the Burgers vector of the original perfect dislocation. The Burgers vectors of the Shockley partials are $\frac{a}{6}\left[11\bar{2}\right]$ and $\frac{a}{6}\left[2\bar{1}\bar{1}\right]$. This dissociation reaction is a consequence of the line energy reduction upon dissociation. As the line energies of dislocations are proportional to the square of their Burgers vectors [6], the sum of the line energies of the partials is lower than the line energy of the perfect dislocation. The equilibrium dissociation width x_0 is reciprocally proportional to the stacking fault energy (SFE) γ_{SF}. For screw dislocations, the following relationship holds [6]:

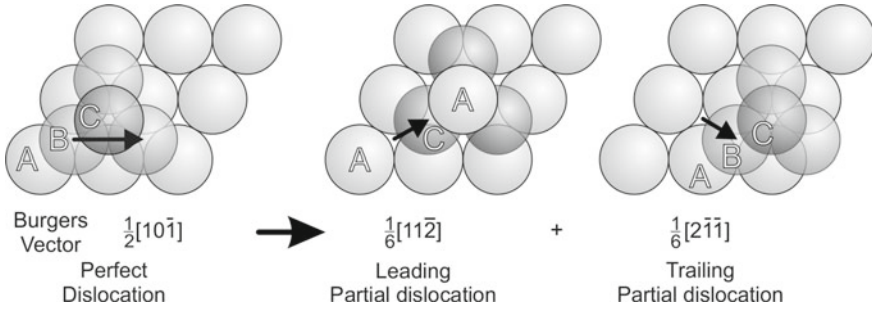$$x_0 = \frac{Gb_p^2}{8\pi\gamma_{SF}}\frac{2-3\nu}{1-\nu} \tag{11.2}$$

Fig. 11.2 Schematic arrangement of the atoms in the close-packed layers in an unfaulted *fcc* crystal (left), after the passage of the leading partial dislocation (middle) and beyond the stacking fault terminated by the trailing partial (right). Adopted from [8]

In (11.2), G is the shear modulus, b_p the magnitude of the Burgers vector of the partial dislocations and ν the Poisson ratio. The reciprocity of the equilibrium dissociation width and SFE means that the dissociation width is small for metals with a high SFE like Al (~200 mJ/m^2 [7]), where it is comparable with the length of the Burgers vector, and large for *fcc* materials with a low SFE, e.g. Ag (~25 mJ/m^2 [7]).

The occurrence of partial dislocations modifies the stacking order of the adjacent atomic planes {111}. In unfaulted *fcc* crystals, the stacking sequence of the close-packed planes {111} along the respective perpendicular direction ⟨111⟩ is *ABCABC* (Fig. 11.2, left). After the passage of the leading partial having the Burgers vector $\frac{a}{6}[11\bar{2}]$, it is modified to *ABCACA* (Fig. 11.2, middle). The passing of the trailing partial with the Burgers vector $\frac{a}{6}[2\bar{1}\bar{1}]$ reconstitutes the original stacking sequence (Fig. 11.2, right). The stacking fault is spanned between the partial dislocations.

Upon loading, the Burgers vectors of the partials interact with the external load, which modifies the movement of the partial dislocations and the widening of the stacking faults. This interaction was described by Copley [9] and Byun [10] as

$$\left[\hat{l} \times \left(\ddot{\tau} \cdot \overrightarrow{b_1}\right)\right] \cdot \hat{x} = \gamma_{SF} - \frac{G}{2\pi x_0}\left[\left(\overrightarrow{b_1} \cdot \hat{l}\right)\left(\overrightarrow{b_2} \cdot \hat{l}\right) + \frac{\left(\overrightarrow{b_1} \times \hat{l}\right)\left(\overrightarrow{b_2} \times \hat{l}\right)}{1 + \nu}\right] + f_0$$

(11.3)

$$\left[\hat{l} \times \left(\ddot{\tau} \cdot \overrightarrow{b_2}\right)\right] \cdot \hat{x} = -\gamma_{SF} + \frac{G}{2\pi x_0}\left[\left(\overrightarrow{b_1} \cdot \hat{l}\right)\left(\overrightarrow{b_2} \cdot \hat{l}\right) + \frac{\left(\overrightarrow{b_1} \times \hat{l}\right)\left(\overrightarrow{b_2} \times \hat{l}\right)}{1 + \nu}\right] + f_0$$

(11.4)

In (11.3) and (11.4), $\overrightarrow{b_1}$ and $\overrightarrow{b_2}$ are the Burgers vectors of the partial dislocations, $\ddot{\tau}$ is the stress tensor, $\hat{l}$ corresponds to the line vector of the dislocation,

Fig. 11.3 Dissociation of a perfect dislocation with the Burgers vector $\vec{b}$ to partial dislocations with the Burgers vectors $\vec{b}_1$ and $\vec{b}_2$ spanning a stacking fault [10]

$$\vec{b} = \vec{b}_1 + \vec{b}_2$$

$$\frac{a}{2}[10\bar{1}] \rightarrow \frac{a}{6}[11\bar{2}] + \frac{a}{6}[2\bar{1}\bar{1}]$$
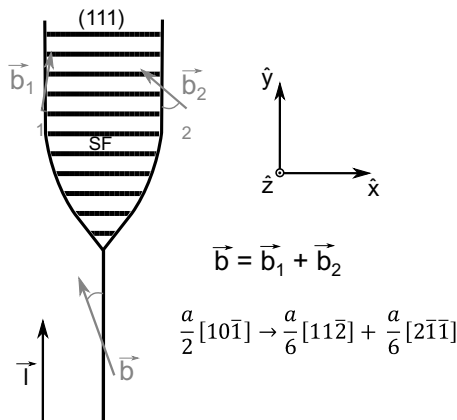
$\hat{x}$ is the unit direction according to the setup in Fig. 11.3, x_0 the separation distance of the partials and f_0 the lattice friction force. The different forces acting on the leading and trailing partial that are induced by the external stress are represented by the left-hand sides of (11.3) and (11.4) [11]. The SFE (γ_{SF}) pulls the partials together, whereas the repulsive interaction force due to their stress fields, i.e., $\pm\frac{G}{2\pi x_0}\left[\left(\vec{b}_1 \cdot \hat{l}\right)\left(\vec{b}_2 \cdot \hat{l}\right) + \frac{\left(\vec{b}_1 \times \hat{l}\right)\left(\vec{b}_2 \times \hat{l}\right)}{1+\nu}\right]$, pushes the partials apart. The lattice friction against the dislocation movement (f_0) is equal for leading and trailing partial dislocation. Using these equations, the equilibrium of the dynamic force under an applied stress can be calculated. The maximum stress effect on the dissociation width is found for screw dislocations. For such dislocations, the separation distance x_0 can be calculated as [10]:

$$x_0 = \frac{(2 - 3\nu)Gb_p^2}{8\pi(1-\nu)\left[\gamma_{SF} - \tau_{zx}b_p/2\right]} \tag{11.5}$$

Consequently, the dissociation distance between the partial dislocations is strongly affected by the SFE (γ_{SF}) and external stress (τ_{zx}). Both effects are illustrated in Fig. 11.4, where the dependence of x_0 on τ_{zx} is plotted for several SFE values. The separation distance increases drastically above a critical stress level [10],

$$\tau_{zx}^{crit} = 2\gamma_{SF}/b_p, \tag{11.6}$$

at which the separation distance in (11.5) approaches infinity. In reality, the stacking fault extends through the entire grain. In materials with lower SFE, wide stacking faults are formed and the critical stress for quasi-infinite dissociation is lower than in materials with higher SFEs. Wide stacking faults are found in the microstructure of deformed austenitic CrMnNi steels and are the reason for their special mechanical behavior. As the SFEs of the austenitic CrMnNi steels with TWIP and TRIP

Fig. 11.4 The dissociation width as a function of the applied stress, plotted for several SFE values according to [10]
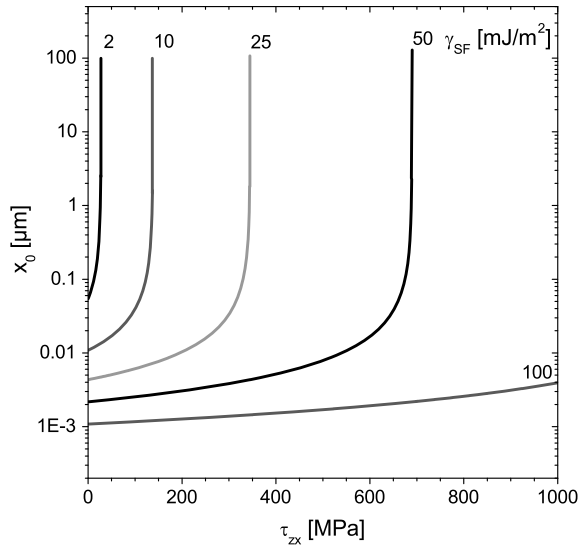
effect range between 2 and 40 mJ/m^2 [12, 13], wide stacking faults form in their microstructure already at low deformations and affect the deformation behavior seriously.

11.2.2 Dislocations and Stacking Faults in Austenitic Steels, Their Configurations and Interactions

The most important microstructure defects in metastable austenite are dislocations with the Burgers vectors $\frac{a}{2}\langle 110 \rangle$ and the stacking faults on the lattice planes {111}. Their configurations and interactions are depicted in the transmission electron microscopy (TEM) micrographs in Fig. 11.5, which were taken in an austenitic steel containing 16 wt% Cr, 7 wt% Mn, 9 wt% Ni, 1 wt% Si, 0.02 wt% C and 0.02 wt% N that was subjected to 2% deformation.

Nearly perfect dislocations (SFs with a very short dissociation width) are visible in area I of Fig. 11.5a, b. They stem from the Frank-Read-like dislocation sources [14]. One example of the Frank-Read source can be seen in the area II of Fig. 11.5a. Larger dissociation is observed for dislocations that are suitably oriented with respect to the applied force. The largely dissociated Shockley partial dislocations form stacking faults that are highlighted by red arrows in Fig. 11.5a. As the partial dislocations can only move on their slip planes, their cross slip to other planes is impeded and only possible, if the partials constrict and recombine. Furthermore, both perfect and partial dislocations are piling up at obstacles during plastic deformation (see, e.g., area I in Fig. 11.5b). These obstacles might be the stress fields produced by immobile dislocations or dislocation clusters as well as the grain boundaries. The pile-ups
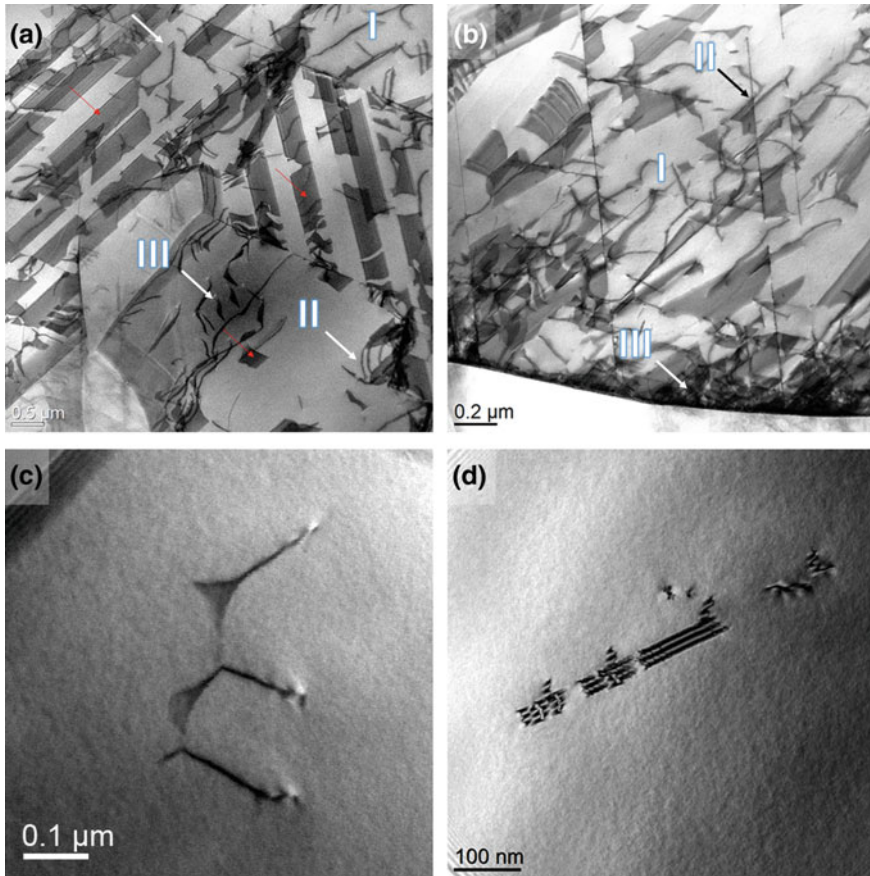
Fig. 11.5 Characteristic dislocation configurations in X2CrMnNi16-7-9 stainless steel having a low stacking fault energy after 2% straining. **a** Depending on the resolved shear stress on individual glide planes, dissociated dislocations form short or wide stacking faults (area III). **b** Beginning of the SF interaction, the deformation band formation, dislocation pile up and Lomer-Cottrell lock formation. **c** Dislocation nodes spanning stacking faults in between. **d** Overlapping stacking faults indicating the SF band formation. Micrographs (**a**) and (**b**) were taken in the scanning TEM mode, micrographs (**c**) and (**d**) in the TEM mode

generate long-range stress fields, which enable further dislocation reactions like the cross-slip of screw dislocations [15].

If multiple slip systems are activated, which is generally the case for plastic deformation of polycrystalline metals, the dislocations can interact with SFs and specific dislocation reactions occur. Dissociated dislocations on intersecting slip planes form Lomer-Cottrell locks [16, 17] as seen in Fig. 11.5b, area II. These locks are generated, when stacking faults on different slip planes encounter. This can be illustrated by the edge-on stacking faults, which seem to stop the SFs on the other slip planes. The normal directions of the edge-on stacking faults lie in

the plane of the TEM sample, thus they are visible just as thin lines in the TEM micrograph. Such locks immobilize SFs on both slip planes, which are now in a sessile configuration, and can cause further dislocation reactions or pile-ups, as the locks are obstacles for following dislocation slip. In Fig. 11.5b, area III, an intense interaction between dislocations and SFs near the grain boundary is obvious. The generation and slip of perfect dislocations, their dissociation, the formation of stacking faults and their widening are the microstructure phenomena that dominate the behavior of the metastable austenitic steels upon plastic deformation [18].

If three dislocations with different Burgers vectors meet on the same slip plane, then they form dislocation nodes [19], as shown in Fig. 11.5c. In the center of such a node, a small stacking fault is produced. This dislocation node behaves like a Lomer-Cottrell lock and persists, therefore, in a stable configuration, which can affect the slip or the formation of following dislocations and SFs [18, 19].

In contrast, the overlap of multiple SFs located on the same slip plane initiates the formation of deformation bands that are depicted in Fig. 11.5d. In this micrograph, the overlap of the parallel stacking faults and the presence of the bordering partial dislocations cause a change in the fringe contrast. The stacking faults accumulated within a deformation band are highly correlated. The deformation bands form first on a primary slip system that possesses the maximum Schmid factor and that experiences the highest shear stress. With increasing applied stress, the deformation bands widen, until they extend over the entire grain size. Concurrently, the increasing applied stress triggers the formation of deformation bands on secondary slip systems. In low-SFE austenitic steels, the formation of deformation bands is the most important deformation mechanism [20].

11.2.3 Arrangement of the Stacking Faults in Austenite: Formation of ε-Martensite and Twinned Austenite

11.2.3.1 Crystallographic and Thermodynamic Aspects of the Stacking Fault Arrangement in *Fcc* Materials

In *fcc* materials, the stacking faults form on the {111} lattice planes via dissociation of perfect dislocations and repulsion of the Shockley partials. As explained in Sect. 11.2.1, the separation distance of partial dislocations and the width of the stacking faults are controlled by the stacking fault energy and by the magnitude of the local shear stress on the glide plane. These two parameters influence, furthermore, the number and/or the density and the arrangement of the stacking faults. At low SF densities, the stacking faults are typically randomly distributed. At (locally) high SF densities, the distances between next stacking faults become much smaller. Consequently, the stacking faults start to arrange.

Two stacking fault configurations deserve a special attention—the arrangement of the stacking faults on **every second** {111} plane and the arrangement of the stacking
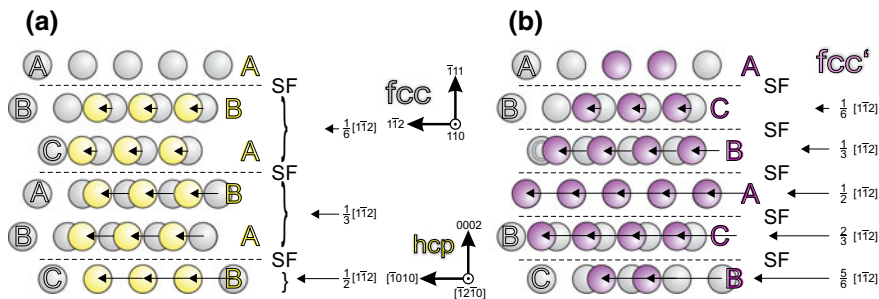
Fig. 11.6 Schemes of special local arrangements of stacking faults (SF) in austenite. **a** The stacking faults are located on every second {111} lattice plane, which leads to the *hcp* stacking. **b** The stacking faults are located on every {111} lattice plane, which leads to the formation of twins (fcc') according to [4]

faults on *every* {111} plane. The arrangement of stacking faults in an *fcc* structure on every second {111} glide plane (Fig. 11.6a) introduces regular *hcp ABABAB* stacking sequence, which is called ε-martensite for the originally austenitic steels. The arrangement of stacking faults on every {111} lattice plane (Fig. 11.6b) reverses the original stacking order *ABCABC* to *CBACBA*, which is denoted as twinning.

From the thermodynamic point of view, the tendency of the stacking faults in austenite to arrange on each second lattice plane {111} is quantified by the Gibbs free energy of the phase transformation of *fcc* γ-austenite to *hcp* ε-martensite ($\Delta G^{\gamma \to \varepsilon}$) [21, 22]. The relationship between $\Delta G^{\gamma \to \varepsilon}$ and the stacking fault energy (γ_{SF}) was described by Olson [21] and Ferreira [23] as

$$\gamma_{SF} = n\rho_A\left(\Delta G^{\gamma \to \varepsilon} + E^{str}\right) + 2\sigma(n) + \sigma_p \tag{11.7}$$

In (11.7), n is the number of the lattice planes {111} that form ε-martensite, ρ_A the molar area density within the close packed lattice planes (mol per area), E^{str} the strain energy resulting from the faulting and $2\sigma(n)$ the interface energy between the faulted structure and the undistorted austenitic matrix (along the $\{111\}_{fcc}$ planes), and σ_p the strain energy of the partial dislocations. The meaning of this formula was discussed in detail by Geissler et al. [22] and De Cooman et al. [12]. The strain energy term (E^{str}) originates from the formation of ε-martensite that is embedded in the austenite matrix. E^{str} is widely accepted to be negligible, because the relative change in the molar volume during the $\gamma \to \varepsilon$ transformation is very small (1.2% in the present case). The dependence of $\sigma(n)$ on n is hardly assessable by experiment, but it can be estimated from the results of ab initio calculations [24]. The contribution of the strain fields of partials (σ_p) can be neglected, in particular if the stacking faults are wide [21].

For isolated stacking faults affecting just two neighboring lattice planes ($n = 2$), (11.7) can be rewritten into the following form that is used for estimation of the SFE from the Gibbs energy of the $\gamma \to \varepsilon$ phase transformation
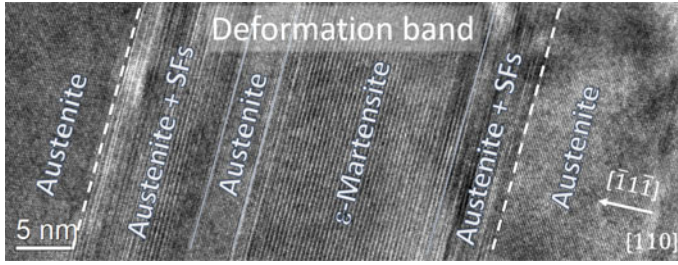
Fig. 11.7 HRTEM image of a 5% strained tensile sample of an X2CrMnNi16-7-6 steel showing various clusters of stacking faults within a deformation band

$$\gamma_{SF}\left[\text{mJ/m}^2\right] = 2(\rho_A \Delta G^{\gamma \to \varepsilon} + \sigma) \tag{11.8}$$

Both parameters $\Delta G^{\gamma \to \varepsilon}$ and σ are strongly dependent on the chemical composition of the steel and on temperature. Still, according to Geissler [22] the term $\rho_A \Delta G^{\gamma \to \varepsilon}$ is approximately one order of magnitude larger than the contribution of the interface energy, $\rho_A \Delta G^{\gamma \to \varepsilon} \cong 5 - 50 \, \text{mJ/m}^2$ versus $\sigma \cong 0.1 - 27 \, \text{mJ/m}^2$, despite the huge span of values available in literature for austenitic steels [22, 25, 26]. It is worth noting that the highest interface energies reported in literature for austenitic steels are not necessarily physically reasonable, because the interfaces between ε-martensite and austenite are almost perfectly heteroepitaxial. Thus, the term $\rho_A \Delta G^{\gamma \to \varepsilon}$ is the most important parameter influencing the stacking fault energy.

It is known from experiments that the distribution of SFs is not homogeneous, as the SFs are typically arranged in deformation bands in plastically deformed samples (Fig. 11.7). This local clustering of SFs has manifold reasons, but most of them are related to a localized nucleation of SFs at stress concentrations, which occurs through the dislocation interactions, local chemical inhomogeneities, or at crystallite boundaries [12].

The stress relaxation through the formation of SFs in austenite is connected with a lattice shear deformation (γ), which is proportional to the magnitude of the Burgers vector of the partial dislocations, $\left|\vec{b}_p\right| = a\left|\left[1\bar{1}2\right]\right|/6$, and which scales with the distance between the next SFs as $\gamma = \left|\vec{b}_p\right|/(n_d d_{111})$. a is the lattice parameter of austenite, $d_{111} = a/\sqrt{3}$ the distance of the close packed lattice planes (neglecting a change of d_{111} near the partials) and n_d the SF distance expressed in the units of d_{111}. The largest shear deformations are achieved in ε-martensite and in twinned austenite. For ε-martensite, where the SFs appear after each second lattice plane $\{111\}$, the lattice shear deformation is about $\gamma_{hcp} = \frac{a}{6}\left|\left[1\bar{1}2\right]\right|/(2d_{111}) = \sqrt{2}/4$. For twins, the lattice shear is twice as large, $\gamma_{twin} = \frac{a}{6}\left|\left[1\bar{1}2\right]\right|/d_{111} = \sqrt{2}/2$, because the SFs are present on each close packed lattice plane. Consequently, the formation of domains, which contain either hexagonally ordered close packed planes of austenite (basal planes of ε-martensite) or twinned austenite, is the most effective way to reduce the local stress concentrations. These domains, which are typically located within

the deformation bands, are fully crystallographically coherent with the austenitic matrix along the respective $\langle 111 \rangle_{fcc}$ or $\langle 0001 \rangle_{hcp}$ direction but incoherent in the perpendicular directions, where the SFs are confined by partial dislocations.

The occurrence of the local stress concentrations in austenitic steels is expected to rise with increasing SFE. According to the stacking fault model from Sect. 11.2.1, the shear stress needed to separate the partials in SFs increases with increasing SFE [10]. Assuming that the amplitude of the local stress concentrations increases if the overall stress level increases, more intense stress concentrations and strongly clustered SFs will appear in austenite with a higher SFE. Very low SFE, in contrast, will facilitate the widening of SFs already at a low overall stress level. This mechanism will prevent strong stress concentrations and local arrangement of the SFs.

11.2.3.2   Detection of the Stacking Faults and Their Arrangements by Diffraction Methods

The impact of stacking faults (SFs) on the diffraction patterns of *fcc* metals was described by Wilson [27], Paterson [28], Warren and Warekois [29] and Warren [30]. This description comprises an anisotropic (i.e., *hkl*-dependent) shift of the diffraction lines, their anisotropic broadening and asymmetry. In the approaches above, the faulting of an *fcc* structure is described as a change in the regular sequence of the lattice planes {111} along the respective normal direction ⟨111⟩. The translation vectors of the regular and faulted *fcc* stacking, $\vec{t} = \left(\frac{1}{3} a_h, \frac{2}{3} a_h, \frac{1}{3} c_h \right)$ and $\vec{t}_| = \left(\frac{2}{3} a_h, \frac{1}{3} a_h, \frac{1}{3} c_h \right)$, respectively, are typically defined in the hexagonal coordinate system obeying the orientation relationship $\left[11\bar{2}0 \right]_{hcp} \parallel \left[1\bar{1}0 \right]_{fcc}$ and $(0001)_{hcp} \parallel (111)_{fcc}$ with respect to the cubic system (Fig. 11.8). The hexagonal lattice parameters a_{hcp} and c_{hcp} are related to the cubic one (a_{fcc}) as

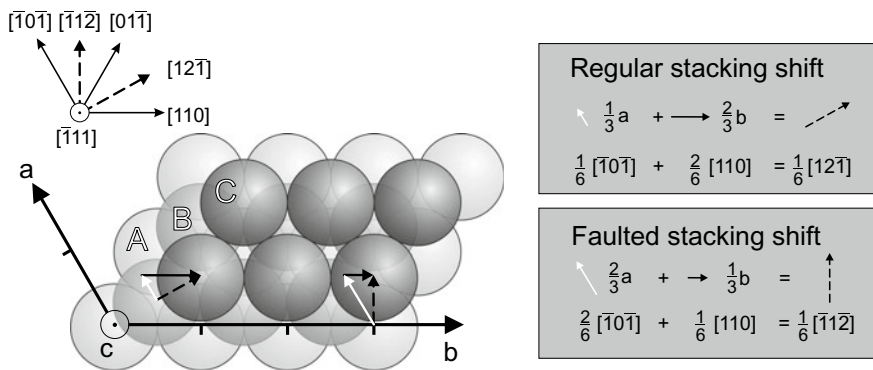$$a_{hcp} = a_{fcc}/\sqrt{2} \text{ and } c_{hcp} = 2a_{fcc}/\sqrt{3} \qquad (11.9)$$

Fig. 11.8 Description of the in-plane shift in the *fcc* lattice in a hexagonal coordinate system as stacking sequence of {111} austenite lattice planes. Adopted from [31]

Martin et al. [31] simulated the effect of the layer stacking on the powder X-ray diffraction (PXRD) patterns using the DIFFaX routine [32] for different stacking fault configurations. The relevant stacking faults configurations are summarized in Table 11.1, the corresponding diffraction patterns are plotted in Fig. 11.9.

As long as the regular *fcc* stacking is maintained ($P_{regular} = 1$), only the diffraction lines corresponding to the *fcc* structure appear (black curve in Fig. 11.9a). The

Table 11.1 Overview of the SF sequences that were used for the DIFFaX simulation (Fig. 11.9) of the PXRD patterns

Sequence of the lattice planes	Probability	Microstructural interpretation
…ABC…	$P_{regular}$	Relative amount of undistorted *fcc* phase
…CAB$_\perp$ABC…	P_{intr}	Relative amount of isolated intrinsic (single) SFs
…CAB$_\perp$A$_\perp$CAB…	P_{extr}	Relative amount of isolated extrinsic (double) SFs
…CAB$_\perp$AB$_\perp$ABC…	P_{hcp}	Relative amount of narrowly spaced SFs appearing repetitively after two lattice planes $\{111\}_{fcc}$
…CAB$_\perp$A$_\perp$C$_\perp$B$_\perp$…	P_{twin}	Relative amount of twins (SFs appearing repetitively after each lattice plane $\{111\}_{fcc}$)
…CAB$_\perp$A$_\perp$C$_\perp$B$_\perp$…	P_{tl}	Extent of the twins (tl—twin length)

The sequence of lattice planes is related to the *fcc* lattice planes $\{111\}$. The appearance of a SF is depicted by the symbol $\perp$. The DIFFaX probability is denoted by the respective symbol P
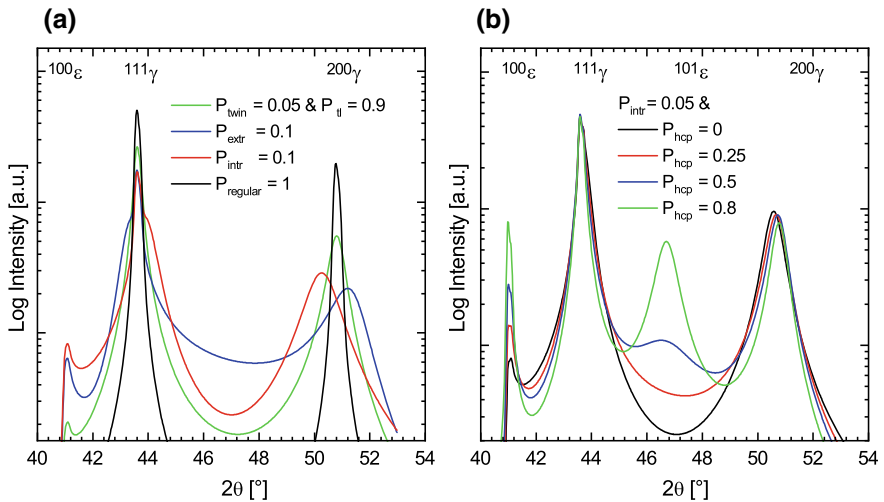

Fig. 11.9 Influence of the stacking fault arrangements on the diffraction pattern: **a** Effect of the isolated SFs and specific SF arrangements on the diffraction pattern, **b** influence of increasing probability (P_{hcp}) for SF arrangements on every second $\{111\}$ glide plane forming hexagonal intensities

presence of isolated intrinsic and extrinsic SFs leads to the line shift and to the line broadening (Fig. 11.9a). Extrinsic SFs and twins make the diffraction profiles strongly asymmetric. According to the Warren theory [30], the line shift caused by the isolated intrinsic stacking faults depends on the diffraction indices (*hkl*) like

$$\Delta 2\theta(°) = 2 \cdot \frac{180°}{\pi} \cdot \frac{\sqrt{3}\alpha}{4\pi} \cdot \frac{\sum_{(\text{affected})} \pm (h + k + l)}{(h^2 + k^2 + l^2) m_{hkl}}, \qquad (11.10)$$

where α is the probability of the occurrence of the isolated intrinsic SFs and m_{hkl} the multiplicity of the lattice planes {*hkl*}. Concurrently, the occurrence of isolated (intrinsic and extrinsic) SFs breaks the coherence of the parts of the crystal structure, which are mutually separated by the stacking faults. This loss of the coherence leads to a line broadening, which can be written in the reciprocal space units as

$$\Delta d_{hkl}^* = \frac{1}{D} + \frac{1.5\alpha + \beta}{a} \sum_{(\text{affected})} \frac{|h + k + l|}{m_{hkl}\sqrt{h^2 + k^2 + l^2}} \qquad (11.11)$$

In (11.11), D is the average crystallite size, β the density of extrinsic SFs and a the cubic lattice parameter. The meaning of other symbols is the same like in (11.10). In both equations, the summations are performed over the indices of the diffraction lines, which are affected by the stacking faults, i.e., for $(h + k + l) \bmod 3 \neq 0$. In (11.10), the positive sign applies for $(h + k + l) \bmod 3 = 1$, the negative one for $(h + k + l) \bmod 3 = 2$.

In contrast to the isolated SFs and twins, SFs appearing repetitively after two lattice planes cause a marginal shift and broadening of the diffraction lines (Fig. 11.9b), but they imitate a hexagonal crystal structure, which is known as ε-martensite in the transformed austenite. Thus, these correlated SFs are not recognized by the diffraction methods as SFs in austenite but as a new phase. The DIFFaX model was tested on the diffraction pattern of a fine-grained sample of an X2CrMnNi16-6-6 TRIP steel that was compressed to 15%. The best agreement between the measured and simulated diffraction patterns was achieved with the probabilities $P_{\text{intr}} = 0.018$, $P_{hcp} = 0.9$, $P_{\text{twin}} = 0.04$ and $P_{\text{tl}} = 0.96$. The successful modelling of the measured XRD pattern using the SF model shows that faulted austenite and ε-martensite present in the microstructure of plastically deformed TRIP steels can be described using specific SF configurations.

Alternatively, the microstructure of deformed steel samples can be described in terms of microstructure components (austenite, ε-martensite and α'-martensite) and microstructure features (dislocation densities and SF probabilities in relevant phases) that are available in most microstructure models used for the whole pattern refinement, i.e., for the Rietveld-like refinement of the XRD patterns. The individual phases (*fcc* austenite, *hcp* ε-martensite and *bcc* α'-martensite) are described using their intrinsic (non-disturbed) crystal structures. The effect of SFs in austenite on the line positions is quantified using (11.10), the effect of SFs in austenite on the line broadening using (11.11) and the effect of SFs in ε-martensite on the line broadening using

(11.14), see Sect. 11.4. The effect of perfect dislocations on the line broadening is
described for all phases using (11.15).

The Rietveld refinement of the diffraction pattern of the fine-grained sample
X2CrMnNi16-6-6 compressed to 15%, cf. previous simulation using the DIFFaX
model, revealed an intrinsic stacking fault probability in ε-martensite of about 10%,
which agrees well with the value of $1 - P_{hcp}$ obtained from the DIFFaX model.
The volume faction of ε-martensite correlates directly with P_{hcp}. In the austenite,
the intrinsic and extrinsic SF probabilities calculated using the DIFFaX model and
the Warren model can be compared directly as well. The parameter P_{twin} can hardly
be compared with the microstructure parameters obtained from the Warren model,
because the twinning does not cause any shift of the diffraction lines but only a line
broadening, see (11.11). However, as it can be seen from (11.11), the densities of
intrinsic (isolated) SFs (α) and extrinsic SFs (β) terminating the twins cannot be
determined simultaneously solely from the line broadening, but only in conjunction
with the analysis of the line shift, or from the line asymmetry [30]. However, as the
density of the twin boundaries in the steels under study is much lower than the density
of intrinsic SFs, it cannot be determined reliably using the combined analysis of the
line shift and line broadening. The analysis of the line asymmetry fails as well, as
the asymmetry of the diffraction lines is not very pronounced [33].

Another result of the Rietveld refinement was that the distance between the
adjacent $\{111\}_{fcc}$ lattice planes within the faulted stacking sequences was smaller
than the interplanar spacing within the regular stacking sequences. Consequently,
the ε-martensite had the c/a ratio of 1.62, which is slightly below the value of
$c/a = 2\sqrt{2/3} = 1.633$ that corresponds to a pseudo-cubic hcp crystal structure
with $a = a^{fcc}/\sqrt{2}$ and $c = 2d_{111}^{fcc} = 2a^{fcc}/\sqrt{3}$.

11.2.3.3 Coexistence of Different Stacking Fault Arrangements: Continuous Transition Between ε-Martensite and Twinning

The coexistence of different stacking fault arrangements in highly alloyed metastable
austenitic steels with a SFE of approx. 20 mJ/m^2 was confirmed by X-ray diffraction
(see previous Section) that found isolated stacking faults together with hexagonal
faulted sequences and twins in the samples under study. The local nature of the
stacking fault clusters was revealed by electron backscatter diffraction in a scanning
electron microscope (EBSD/SEM) and by transmission electron microscopy with
high resolution (HRTEM). On a mesoscopic scale, EBSD disclosed that the crystal
structure defects are concentrated in the deformation bands, which contain typically
ε-martensite slabs and deformation twins (Fig. 11.10). The character of the defor-
mation bands (predominantly ε-martensite or mainly deformation twins) depends
generally on the SFE and deformation state. The occurrence of these deformation
bands varies with the crystallographic orientation of the originally austenitic grains
with respect to the deformation direction.

On the atomic scale, the coexistence of the different stacking fault arrangements
was proven by HRTEM that was complemented by the fast Fourier transform (FFT) of
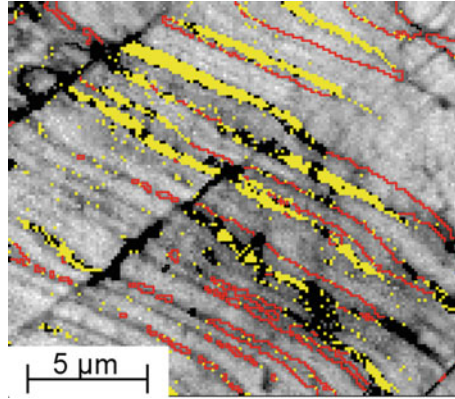
Fig. 11.10 EBSD mapping of deformation bands in compressed X5CrMnNi16-6-9 steel, austenite in grey, ε-martensite in yellow, twin boundaries in red, unindexed pixels in black. Adopted from [34]
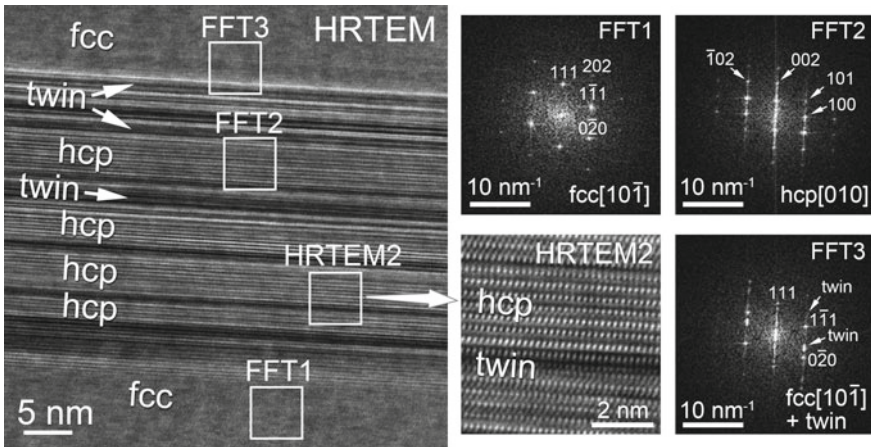

Fig. 11.11 HRTEM image of a deformation band, where atomic arrangements of both twins and ε-martensite are found coexisting in close vicinity

the HRTEM micrographs. Figure 11.11 illustrates the different stacking sequences of the former $\{111\}_{fcc}$ lattice planes, which can be described as an irregular ordering of stacking faults. Extended sequences $AB_\perp AB_\perp AB_\perp AB$ of the lattice planes $\{111\}_{fcc}$ are interpreted as hcp ε-martensite, extended sequences $ABCAB_\perp A_\perp C_\perp B_\perp A_\perp C_\perp$ as twins. The irregular sequences of SFs produce streaks in the reciprocal lattice of austenite along the faulted $\langle 111 \rangle_{fcc}$ direction, which include the reciprocal lattice points of ε-martensite (see FFT2 in Figs. 11.11 and 11.12b). The streaks stem from superimposed truncation rods produced by thin slabs of faulted austenite [28, 35, 36]. The presence of extended slabs of ε-martensite or extended twins leads to the
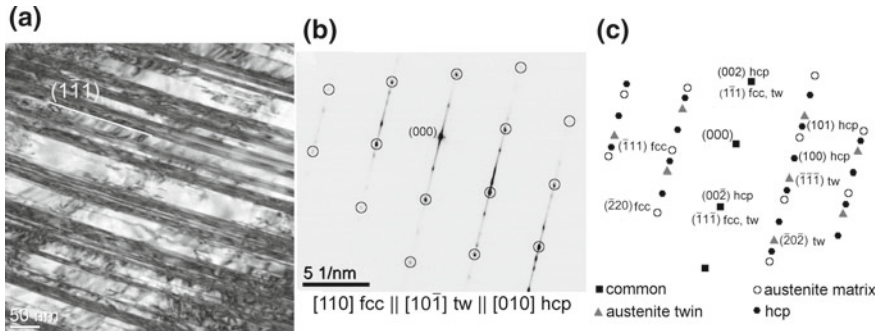
Fig. 11.12 TEM characterization of deformation bands in PM X5CrMnNi16-6-9 steel. **a** Bright-field image of parallel deformation bands, **b** corresponding SAED, recorded with a 200 nm aperture, **c** indexing of spots assigned to austenite matrix, twin and ε-martensite. Adopted from [34]

fragmentation of the streaks and to the formation of separated diffraction spots that correspond to ε-martensite or to twins in austenite (see FFT2 and FFT3 in Fig. 11.11). These microstructure features are interpreted in a very similar way by all diffraction methods, i.e., EBSD (Fig. 11.10), selected area electron diffraction (SAED) in TEM (Fig. 11.12) and XRD (Fig. 11.9).

The crystallographic explanation of these diffraction phenomena is based on the stacking fault models from Figs. 11.6 and 11.7, and on the orientation relationships between austenite, ε-martensite and twinned austenite that can be described as $(0001)_{hcp} \parallel (1\bar{1}1)_{fcc} \parallel (1\bar{1}1)_{\text{twin}}$ and $[01\bar{1}0]_{hcp} \parallel [110]_{fcc} \parallel [10\bar{1}]_{\text{twin}}$, cf. Fig. 11.12b, c. The deformation bands visible in the TEM micrograph (Fig. 11.12a) contain remainders of the austenite matrix, uncorrelated SFs and areas, which are interpreted as ε-martensite or as twins in austenite. In the SAED pattern (Fig. 11.12b), the remainders of the austenite matrix, the ε-martensite areas and the twinned austenite produce intense diffraction spots, the uncorrelated SFs streaks along the $(1\bar{1}1)_{fcc}$ reciprocal space direction.

From the thermodynamic point of view, the simultaneous occurrence of twinned austenite and ε-martensite can be discussed in terms of SFE and interface energy [22]. In the case of a low thermodynamic driving force ($\Delta G^{\gamma \to \varepsilon} \cong 0$, cf. Sect. 11.2.3.1), all arrangements of stacking faults corresponding to isolated intrinsic and extrinsic SFs, ε-martensite and twins result in the same overall energy. Therefore, the transition between the transformation-induced plasticity (TRIP) and the twinning-induced plasticity (TWIP) is continuous. Assuming that there are no other obstacles for the phase transition, the TRIP effect and the generation of a local hexagonal stacking sequence are preferred for $\Delta G^{\gamma \to \varepsilon} < 0$, while for $\Delta G^{\gamma \to \varepsilon} > 0$, the twinning dominates.

An important consequence of this microstructure model is an improved atomistic description of the ε-martensite formation. Although SFs were always regarded as nucleation precursor [21] of the ε-martensite formation, the ε-martensite has been treated as a metastable martensitic phase occurring along the $\gamma \to \varepsilon \to \alpha'$ transformation path [37, 38] and as a product of bulk martensitic transformation of austenite

[39]. The current understanding of ε-martensite, which evolves during plastic deformation of austenite, is that it is rather a heavily faulted austenite than a distinct phase.

Using electron microscopy, the ε-martensite was found to appear within deformation bands [31, 40], where a high density of stacking faults is present. Consequently, the deformations bands and hence the ε-martensite form during the plastic deformation of austenite, when a low SFE facilitates the SF formation as a competing mechanism to the dislocation mobility. On the other hand, the deformation bands and the ε-martensite act as repositories of dissociated dislocations, which are bound to their slip planes. Hence, the dynamic recovery is inhibited, as the annihilation would be possible only for perfect dislocations, which are not stable, as their dissociation is facilitated by the low SFE.

11.2.3.4   Thermal Stability of the Deformation-Induced ε-Martensite

The defective character of ε-martensite was confirmed by the thermal behavior of the X2CrMnNi16-7-6 TRIP steel, which was deformed to 25% true compressive deformation at room temperature. In this deformation state, the originally austenitic steel contained 51 vol% *fcc* austenite, 30 vol% *bcc* α'-martensite and 19 vol% *hcp* ε-martensite. The in situ high-temperature XRD measurement carried out upon heating revealed that the ε-martensite disappears between 250 and 350 °C, while the α'-martensite vanishes at approximately 600 °C (Fig. 11.13a). The transformation of α'-martensite to γ-austenite was confirmed by differential scanning calorimetry (DSC), which showed a distinct maximum of the heat flux between 500 and 600 °C (Fig. 11.13b), that is in agreement with the existence range of the *bcc* phase from Fig. 11.13c. The σ-phase from the phase diagram was not observed, because its formation was kinetically inhibited through the rapid quenching.
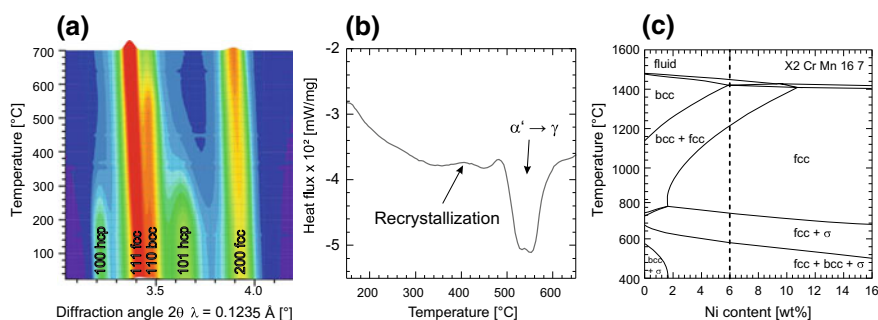

Fig. 11.13 Thermal behavior of an X2CrMnNi16-7-6 TRIP steel deformed to 25%. **a** X-ray synchrotron diffraction patterns recorded during continuous heating. The intensities are plotted in logarithmic scale. **b** The DSC heat flux signal during continuous heating at 10 K/min. **c** Isopleth section of the X2CrMnNi16-7-x steel for Ni concentrations between 0 and 15%

The ε-martensite is no thermodynamically stable phase, thus its existence cannot be proven by the phase diagram. Also in the DSC measurement, no pronounced signal related to the back transformation of ε-martensite was detected. The small differences in the heat flux measured between 250 and 350 °C are comparable with the DSC signal that originates from recrystallization, i.e., from the annihilation of the crystal structure defects in austenite [41, 42]. The absence of a pronounced DSC signal stemming from the dissolution of ε-martensite confirms that the reverse transformation of ε-martensite to austenite happens via 'unfaulting' [43], for which no pronounced diffusion activity of the lattice atoms is needed.

The recovery of austenite and the disappearance of SFs upon heating are supported by the increase of the SFE with increasing temperature (δSFE/δT), which is between 0.05 and 0.1 mJ/(m^{2}K) [7, 44]. Thus, the energy stored in the existing stacking faults increases with increasing temperature. The increase of SFE produces a significant constriction force that acts on partial dislocations and reduces the width of the stacking faults. Large stacking faults collapse and the SFs arrangement in deformation bands disappears in favor of the recovery of original austenite.

11.2.3.5 Phase Transformations in Austenitic Steels Under High Pressure

Pure iron is known to undergo a $bcc \rightarrow hcp$ transformation during hydrostatic compression between 8 and 13 GPa and room temperature [45–48]. This transition was explained theoretically by a change of the magnetic state of iron from a ferromagnetic one to a non-magnetic or antiferromagnetic one, when hydrostatic pressure is applied [49–51]. In order to find out possible analogies between the formation of ε-martensite in austenitic steels and the hcp high-pressure phase in ferrite under hydrostatic pressure, in situ high-pressure synchrotron diffraction experiments up to 18 GPa were carried out on a fcc TRIP steel using a multi-anvil apparatus [52].

For this purpose, small cylinders of the austenitic X2 CrMnNi16-7-6 TRIP steel were encapsulated in an MgO container together with indium that served as a pressure standard, and compressed by WC anvils. The XRD patterns were collected in the energy-dispersive mode at the diffraction angle $2\theta = 3.1557°$ (calibrated by a LaB$_6$ standard). An excerpt of the analyzed raw data is displayed in Fig. 11.14a. The effective applied pressure was calculated from the change of the specific volume of the reference material.

In contrast to ferrite (pure iron), where the phase transition occurs between 8 and 13 GPa, the hcp phase in the TRIP steel appeared already at approx. 0.5 GPa [52]. Its amount was about 20 vol%. This earlier phase transformation may be facilitated by shear stress components, which result from the strong crystallographic anisotropy of the elastic constants of austenite and from the polycrystalline nature of the investigated sample. The local shear stress components and the stress concentrations at the grain boundaries are released by local plastic deformation involving dislocation slip and formation of stacking faults and deformation bands, which support the martensitic transformation of fcc austenite to hcp ε-martensite. For these reasons, the
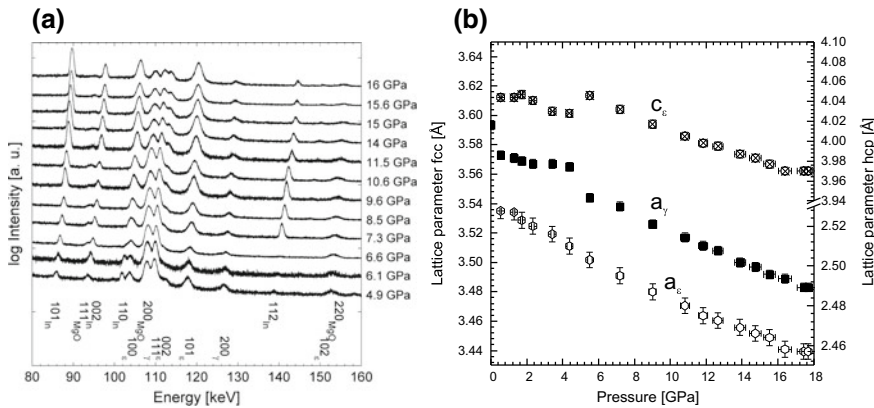
Fig. 11.14 Evolution of the ε-martensite formation at increasing hydrostatic compression. **a** Raw data of the compression experiments show a clear increase of the *hcp* phase fraction with increasing hydrostatic pressure. **b** Evolution of the lattice parameters. Adopted from [52]
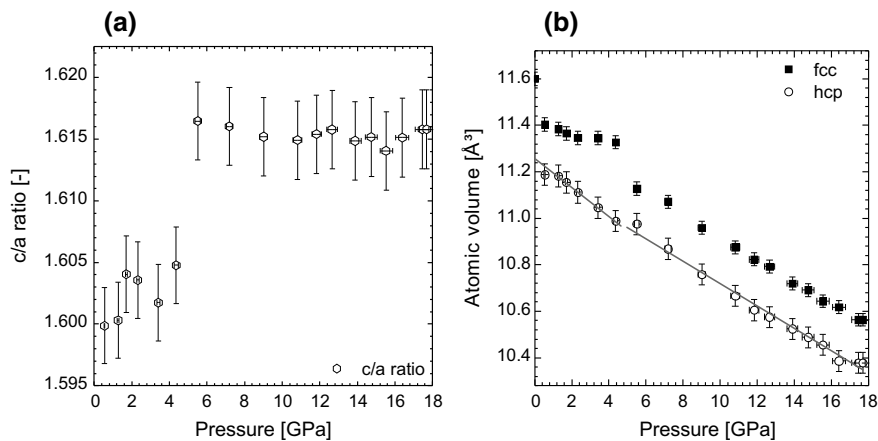

Fig. 11.15 Structural changes in *fcc* austenite and *hcp* ε-martensite during hydrostatic compression. **a** Evolution of the *c/a* ratio in *hcp* ε-martensite during compression. **b** Change of the atomic volume (volume per Fe atom in the unit cell) in both phases. According to [52]

hcp phase found in austenite subjected to high hydrostatic pressures above 5 GPa is inherently of the same nature as the deformation-induced ε-martensite, which is produced by uniaxial loading. Still, up to the hydrostatic pressure of 5 GPa the *c/a* ratio calculated from the lattice parameters of the *hcp* phase (Fig. 11.14b) was between 1.600 and 1.605 (Fig. 11.15a) [52], which agrees well with the *c/a* = 1.602 − 1.603 reported for the high-pressure phase of iron by Mao et al. [46], Takahashi et al. [47] and Giles et al. [48].

Above the hydrostatic pressure of ~6 GPa, more than 50 vol% of the sample transformed to ε-martensite. This phase transformation was accompanied by an apparently higher compressibility of the austenite and by an abrupt increase of the c/a ratio from ~1.605 to 1.617, which was caused mainly by the expansion of the hexagonal lattice parameter c (Fig. 11.14b). A generally smaller specific volume of the *hcp* phase hexagonal structure in comparison with the *fcc* phase together with the higher compressibility of austenite and a faster reduction of its volume at the pressures above 6 GPa (Fig. 11.15b) can be, according to Le Chatelier's principle [53, 54], a significant driving force for the phase transformation. The value of $c/a = 1.617$ approaches the c/a ratio in ε-martensite produced by plastic deformation. The change of the c/a ratio from 1.605 to 1.617 is possibly related to the change in the ordering of magnetic moments. As the change of the c/a ratio is accompanied by a slight expansion of the elementary cell of the *hcp* ε-martensite at ~6 GPa, a transition from the paramagnetic to the antiferromagnetic state is expected.

11.3 Formation of α'-Martensite

The formation of *bcc* α'-martensite is a characteristic feature of metastable austenitic steels with a low SFE that has a prominent effect on their mechanical properties. The α'-martensite formation is triggered by cooling the metastable austenite below a critical temperature and enhanced by mechanical load [55]. The driving force of the $\gamma \rightarrow \alpha'$ transformation is proportional to the difference in the Gibbs energies of the *fcc* and the *bcc* phase, $\Delta G^{\gamma \rightarrow \alpha'}$, which, in turn, depends on temperature and on the chemical composition of the steel [56]. In metastable austenite, $\Delta G^{\gamma \rightarrow \alpha'}$ is negative below the thermodynamic equilibrium temperature T_0, which is about 600 °C (see Fig. 11.13c) for the austenitic TRIP steel X3CrMnNi16-7-6.

However, as the transformation temperature, which is observed experimentally, e.g., by dilatometry, is affected by several factors, the martensite start temperature (M_S) is introduced that describes the real onset of the phase transformation in terms of a characteristic amount of undercooling. The difference between T_0 and M_S is caused by the obstruction of the $\gamma \rightarrow \alpha'$ transformation—mainly through the formation of the γ/α' interfaces and through the lattice strain resulting from the approx. 2% volume expansion during the $\gamma \rightarrow \alpha'$ transformation. The formation energy of the γ/α' interface and the lattice strain produced by the phase transformation must be compensated by a sufficiently negative value of $\Delta G^{\gamma \rightarrow \alpha'}$. The plastic deformation of austenite caused by external force may aid the martensitic transformation by imposing shear stress that acts as mechanical driving force [55] and by providing favorable nucleation sites for α'-martensite. Thus, a threshold temperature (M_D), below which the deformation-induced martensitic transformation occurs, is located between M_S and T_0.

In high alloy metastable austenitic steels, which possess a low SFE (< 20 mJ/m^2 [12]) and which show the TRIP effect [57], the transformation path follows mostly the $\gamma \rightarrow \varepsilon \rightarrow \alpha'$ sequence [21, 58, 59]. This sequence implies that α'-martensite is

formed predominantly by shearing the previously formed ε-martensite. This particular conclusion is confirmed by the SEM/EBSD micrographs of plastically deformed TRIP steels, which show that α'-martensite arises mainly at the intersections of deformation bands containing ε-martensite (see left-hand side of Fig. 11.16). The stages of the phase transformation are schematically depicted in the middle column and on the left-hand side of Fig. 11.16. The phase transformation starts with a simple arrangement of stacking faults on parallel {111} lattice planes and the formation of deformation bands (panel (1) in Fig. 11.16). When at a higher strain such deformation bands form on crystallographically equivalent {111} planes and intersect, then the intersections provide, according to the Olson-Cohen model [21, 60], favorable nucleation conditions for α'-martensite (panel (2) in Fig. 11.16). The phase transformation within a deformation band can even be triggered by a single stacking fault appearing on a secondary slip plane that crosses the deformation band (Fig. 11.16 panel (2)) [61–63].

According to the Bogers-Burgers mechanism [64], the $fcc \rightarrow bcc$ transformation can be realized by two shears on different slip planes, which are equal to $a/18[211]$ on
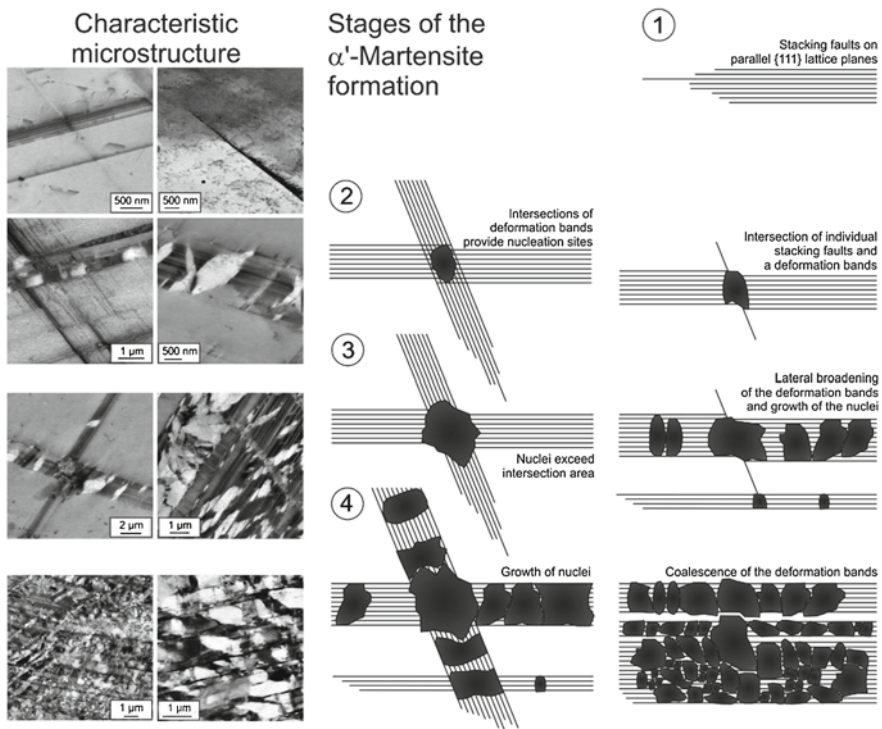

Fig. 11.16 Stages of the deformation-induced α'-martensite transformation in an X2 CrMnNi16-7-6 steel as seen by ECCI (left-hand side), and depicted schematically for nucleation at deformation band intersections (centre) and inside deformation bands (right), respectively

the $(\bar{1}11)$ plane and to $a/12[21\bar{1}]$ on the $(1\bar{1}1)$ plane [60]. The first shear corresponds to one third of the twinning shear; the second shear is equivalent to the shear of partial dislocations passing on every second {111} plane, or within the ε-martensite slab [65]. The resulting local atomic arrangement resembles the *bcc* structure of α'-martensite, and can be described by a hypothetic intersection of a perfect and a faulted ε-martensite bands. The formation of ε-martensite comprises already a shearing (leading to the development of the *hcp* stacking sequences), which reduces significantly the energetic barrier for the α'-martensite nucleation.

Upon further straining, the α'-martensite nuclei grow and eventually outrun the original deformation band at the intersection points (panel (3) in Fig. 11.16). Finally, the α'-martensite nuclei grow together, thus the former deformation bands containing the ε-martensite slabs gradually transform into α'-martensite (panel (4) in Fig. 11.16). Due to the thickening of the α'-martensite regions, the distances between individual deformation bands become smaller and the originally separated α'-martensite regions merge partially, so that entire grains of original austenite transform to α'-martensite.

The mechanism of the α'-martensite formation was confirmed by TEM and FFT/HRTEM (Fig. 11.17). Inside of a deformation band (labelled as (2)), which intersects with few individual SFs but not with a pronounced deformation band, several α'-martensite nuclei (labelled as (3)) were identified. This case was discussed in Fig. 11.16, panel (2), above. In addition to the local phase identification, the FFT/HRTEM patterns from the adjacent regions A, B and C in Fig. 11.17, were used for the analysis of the orientation relationships (ORs) between original austenite (phase 1), faulted ε-martensite (phase 2) and α'-martensite (phase 3). The faulting of austenite and ε-martensite produces diffraction contrasts in the TEM micrograph and perpendicular streaks in the FFT pattern. From the coincidence of the distinct reciprocal lattice points in the FFT/HRTEM patterns, the following parallelisms of
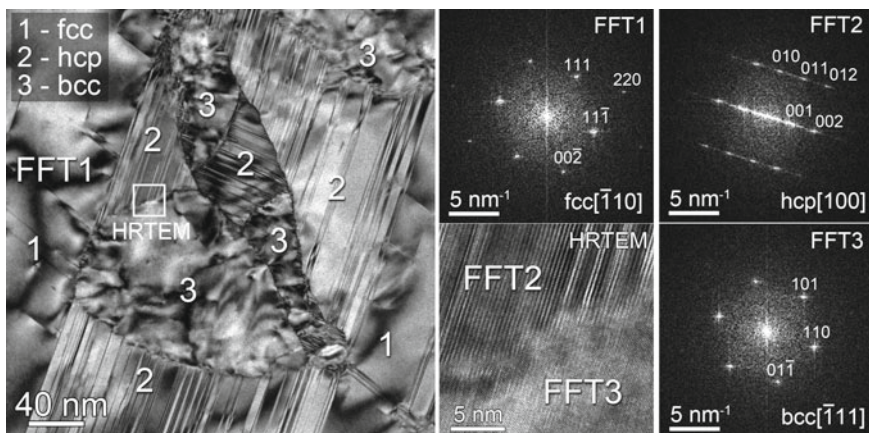

Fig. 11.17 TEM micrograph of the martensitic transformation in a deformation band, FFTs of high-resolution TEM images revealing the local crystal structure and orientation in the marked areas. The crystal structure identified in different regions is indicated by numbers

the close-packed planes and directions were concluded:

$$\left\{11\bar{1}\right\}_{fcc}\|\{001\}_{hcp}\|\{110\}_{bcc} \tag{11.12}$$

$$\left\langle\bar{1}10\right\rangle_{fcc}\|\langle100\rangle_{hcp}\|\left\langle\bar{1}11\right\rangle_{bcc} \tag{11.13}$$

In literature, these relations are known as Kurdjumow-Sachs OR [66] (for the *fcc/bcc* interface) and as Shoji-Nishiyama OR (for the *fcc/hcp* interface) [67]. In particular, the OR between *fcc* austenite and *hcp* ε-martensite corroborates the concept of the formation of ε-martensite by stacking faults.

11.4   Quantification of Microstructure Features and Microstructure Defects in TRIP/TWIP Steels, Determination of the Stacking Fault Energy in Austenite

11.4.1   Experimental Methods for Quantitative Microstructure Analysis

The characteristic microstructure features of the TRIP/TWIP steels are the amounts of original metastable γ-austenite and twinned austenite, ε-martensite and α'-martensite, the size of the grains or crystallites of the respective phase, the densities of microstructure defects (mainly dislocations and stacking faults), the preferred orientations of crystallites and the macroscopic or mesoscopic lattice deformations. The mechanisms of the microstructure defect formation and phase transformations were described in Sects. 11.2 and 11.3. Preferred orientation of crystallites is a result of local lattice rotations occurring during the plastic deformation. Macroscopic (elastic) lattice deformations stem from the external load, which is not relieved by the crystal plasticity. Mesoscopic elastic lattice deformations are induced by the interaction of neighboring grains or phases at their interfaces.

From the historical point of view, the first microstructure feature of interest in the TRIP steels was the amount of α'-martensite, as the progress of the martensitic phase transformation was related to the strength and the strain hardening of these steels [68]. For the quantification of the α'-martensite phase fraction, several methods were established. One of them utilizes the measurement of the magnetic permeability by a magnetic balance (ferritescope). The physical background of this method is that α'-martensite is a ferromagnetic phase, while austenite and ε-martensite are not ferromagnetic. The main drawbacks of the permeability measurement are that it cannot distinguish between α'-martensite and δ-ferrite,[2] and that the magnetization of

---

[2]The δ-ferrite is another ferromagnetic phase that can be retained in austenitic steels as a high-temperature *bcc* phase during the dendritic solidification.

α'-martensite depends on the strain. Hence, the ferritescope must be calibrated using a fully martensitic standard [69]. The advantage of the magnetic measurement is that it covers a large sample volume and provides a good statistics even for coarse-grained cast steels.

As ε-martensite and residual austenite are non-ferromagnetic phases, their amounts are typically quantified using diffraction methods like XRD and EBSD. For the phase identification, γ-austenite is described as an *fcc* phase (structure type Cu) with the lattice parameter about 3.59 Å, ε-martensite as a *hcp* phase (structure type Mg) with the lattice parameters $a \approx 2.54$ Å and $c \approx 4.11$ Å, and α'-martensite as a *bcc* phase (structure type W) with the lattice parameter about 2.87 Å. For the phase quantification, XRD uses the intensity ratios [70]. Nowadays, the phase quantification using XRD is usually carried out by employing the Rietveld analysis of the diffraction pattern [71, 72]. Phase quantification using EBSD is based on the comparison of the respective phase areas.

In comparison to the magnetic measurement, XRD and EBSD probe a significantly smaller sample volume. The penetration depth of X-rays (Cu Kα radiation) in TRIP/TWIP steels is about 8 μm, the irradiated area usually several mm^2. Typical information depth of the backscattered electrons in steels is about 70 nm (at the acceleration voltage of 20 kV), the analyzed area below 1 mm^2. Still, in most cases the amount of α'-martensite determined using XRD agrees very well with the values obtained from the magnetic measurement, as it is illustrated in Fig. 11.18 for several compression steps.

The quantification of the phase fractions using EBSD is generally biased by a low quality of the Kikuchi patterns in the regions that experienced a high local deformation, e.g., within the deformation bands. In such regions, the indexing of the Kikuchi patterns is frequently not possible, thus heavily deformed austenite and ε-martensite are not be considered for the quantitative phase analysis. For this reason, EBSD

Fig. 11.18 Comparison of the results of the ε- and α'-martensite quantification using magnetic measurement, EBSD and XRD. The stress-strain curve (solid line) shows the deformation state of the PM X3CrMnNi16-7-6 steel
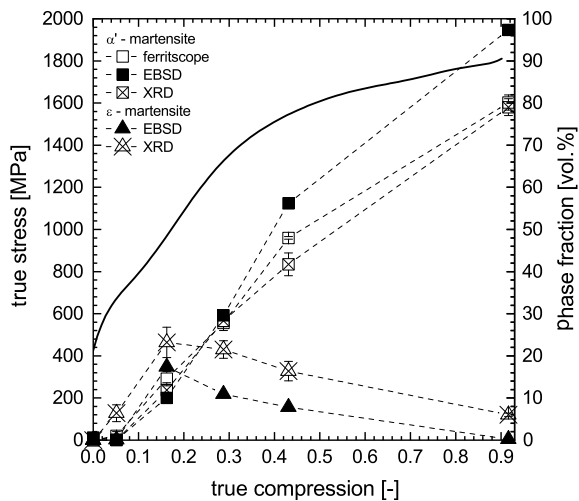
systematically underestimates the amount of ε-martensite, which contains a considerable amount of SFs. Furthermore, thin ε-martensite lamellae having a thickness below 100 nm cannot be resolved by EBSD, because the Kikuchi patterns from the ε-martensite lamellae are superimposed by the Kikuchi pattern from the surrounding (faulted) austenite. Finally, the α'-martensite fraction determined using EBSD in highly strained samples is overestimated at the expense of the deformed austenite, which is not recognized (because not indexed) due to a high defect density. Consequently, XRD provides a better accuracy in determining the ε-martensite fraction than EBSD. The influence of this effect is perceptible in Fig. 11.18, where the results of the quantitative phase analysis using EBSD and XRD are compared.

Another microstructure component, which is important for explanation and modelling of the mechanical behavior of the TWIP steels, is the twinned austenite [12, 73–76]. However, as the strength of the steels is governed rather by the density of the twin boundaries restraining the dislocation slip [75] than by the volume fraction of the twins, the density of the twin boundaries is the relevant quantity, which has to be determined experimentally. However, due to the usually very fine morphology of the twins (thickness ~50 nm), neither SEM nor XRD can quantify the density of the twin boundaries accurately. The typically practiced EBSD orientation mapping [73, 77, 78] cannot account for the very fine twin structure, as its lateral resolution is limited. The twins can be more easily identified by electron channeling contrast (ECC). However, the ECC images are not commonly used as additional information for automated EBSD phase analysis.

The effect of the limited lateral resolution of EBSD on the result of the quantitative microstructure analysis is illustrated in Fig. 11.19. The ECC image reveals twin bundles, which are only partly recognized as twins in the corresponding EBSD mapping. In case of the not recognized twins, the measured Kikuchi pattern is a superposition of the Kikuchi patterns from the matrix and from twins that is indexed according to the dominant diffraction volume, which is the matrix. The only technique, which is capable of resolving the nanoscopic twin structures, is HRTEM (see, e.g., Figure 11.11). However, it is limited to small sampling sizes and therefore it suffers from the statistical unreliability.

The quantification of the twin density in austenite by XRD is difficult, as the twinning causes mainly an *hkl*-dependent asymmetry of the diffraction lines [30]. For low twin densities, the line asymmetry is relatively weak, because the shape of the diffraction lines from the *fcc* phase is dominated by the undisturbed austenite regions, while the contribution of the twins is negligible. Furthermore, the influence of the twinning on the line broadening and shift is small as compared to isolated stacking faults [33].

Still, XRD is capable of quantifying the density of isolated stacking faults in austenite and ε-martensite. In austenite, the isolated stacking faults affect both the positions and the broadening of diffraction lines as described in Sect. 11.2.3.2. In ε-martensite, the presence of isolated stacking faults leads to the broadening of diffraction lines β_{hkl}^{SF} with $h - k = 3n \pm 1$ that is equal to [30, 79]
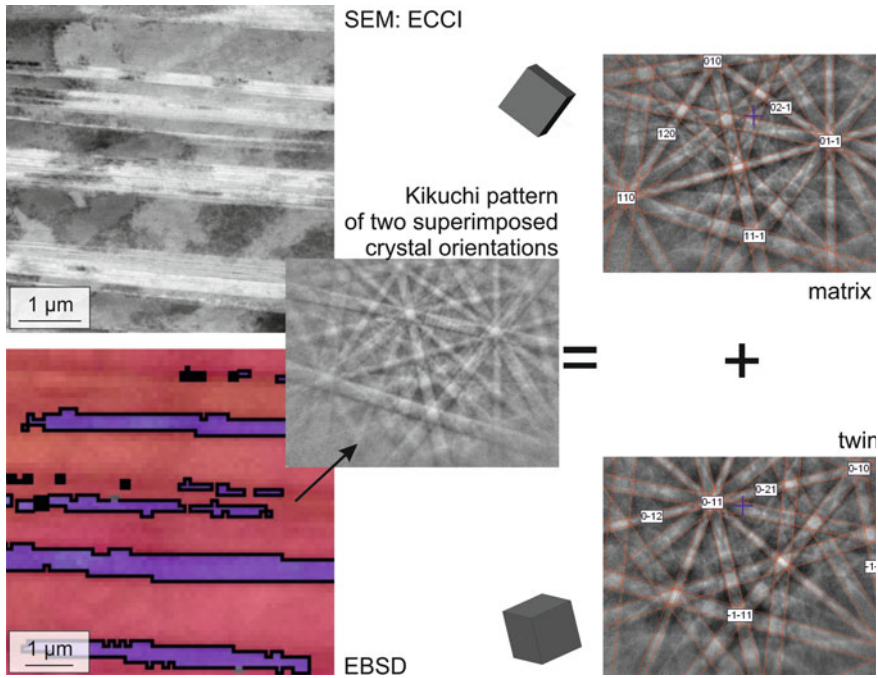
Fig. 11.19 Difficulty of indexing twin bundles by EBSD due to the limited resolution and the superposition of Kikuchi patterns in the fine-scale microstructure

$$\beta_{hkl}^{\text{SF}} = \frac{3l\alpha}{c^2 d_{hkl}^*}, \tag{11.14}$$

where l is the diffraction index, c the hexagonal lattice parameter and d_{hkl}^* the inter-planar spacing in the reciprocal space. The densities of dislocations are determined from the hkl-dependent line broadening as well. The line broadening caused by dislocations is proportional to the square root of the dislocation density (ρ) and to the square root of the contrast factor of dislocations ($\bar{C}_{hkl}$) [80–85]:

$$\beta_{hkl}^{disl} = \sqrt{\frac{\pi}{2}} M \sqrt{\rho} b \sqrt{\bar{C}_{hkl}} d_{hkl}^* \tag{11.15}$$

Further parameters affecting the magnitude of the line broadening in (11.15) are the Wilkens factor M, the Burgers vector b and the length of the reciprocal space vector (d_{hkl}^*). As the contrast factors describe the elastic response of the material on the presence of dislocations, they are basically calculated from the elastic constants of the material under study [82, 83, 86]. Nevertheless, Ungár et al. showed that for cubic and hexagonal materials, the hkl-dependence of the contrast factors must comply with the crystallographic anisotropy of the elastic constants [84, 87]. Therefore, it can be described by the respective crystallographic invariant:

$$\bar{C}_{hkl}^{\text{cub}} = \bar{C}_{100}\left[1 - A\frac{h^2k^2 + k^2l^2 + l^2k^2}{\left(h^2 + k^2 + l^2\right)^2}\right] \tag{11.16}$$

$$\bar{C}_{hkl}^{\text{hex}} = \bar{C}_{hk0} + \frac{\left[2A\left(h^2 + hk + k^2\right) + Bl^2\right]l^2}{\frac{9}{4}\left(ad_{hkl}^*\right)^4} \tag{11.17}$$

The factors *A* and *B* characterize the degree of the crystallographic anisotropy. In the computer routines employed for the Rietveld refinement of the XRD patterns, the dependence of the dislocation-induced line broadening on the diffraction indices is calculated using the Popa model [88].

11.4.2 Methods for Determination of the Stacking Fault Energy (SFE) in fcc Crystals

As discussed above, the knowledge of the SFE is crucial for the prediction of the deformation behavior of *fcc* metals and alloys, because it determines the occurring deformation mechanisms and consequently the strain hardening. In literature, various attempts to measure the SFE are reported that are mostly based on TEM or XRD methods. The most common TEM technique is the measurement of the separation distance of the partial dislocations [89–92]. Usually, weak beam imaging is utilized to identify the dissociation distance between the partials, which amounts several nanometers and depends on the dislocation character (edge or screw). Indeed, detectable dissociation widths are found in materials with a relatively low SFE only. Another TEM approach examines extended dislocation nodes, in particular the curvature radius, from which the SFE is concluded [93–96]. Some problems might arise from the delicate preparation of thin TEM foils, which can produce undefined strains in the area close to the investigated triangle dislocation node. Another source of systematic errors is a high sensitivity of the width of the dislocation nodes to the local concentration of the alloying atoms [90]. A general drawback of TEM is its limited statistical relevance.

The first technique for the SFE determination using XRD was developed by Dillamore [97, 98], who proposed obtaining SFE from the degree of the preferred orientation of crystallites, and directly from the ratio of two different texture components extracted from the pole figures. The idea behind this approach is that the formation of a crystallographic texture requires cross slip of perfect dislocations, which is a competing mechanism to the dislocation dissociation driven by a low SFE. This method can be applied for a wide range of SFEs, but is purely empirical and offers only a rough estimation of the SFE.

A more reliable XRD technique for the SFE determination is based on the analysis of the broadening and shift of the diffraction lines in XRD patterns of plastically deformed samples [99, 100]. Within this approach, the SFE (γ_{SF}) is proportional to the ratio of the squared dislocation-induced microstrain measured in the $\langle 111 \rangle$

direction $\left(\left\langle\varepsilon_{111}^2\right\rangle\right)$ and the SF probability (α):

$$\gamma_{\text{SF}} = \frac{K_{111}\omega_0 G_{111} a_0}{\pi\sqrt{3}} \cdot \frac{\left\langle\varepsilon_{111}^2\right\rangle}{\alpha} \tag{11.18}$$

The microstrain and the SF probability are determined from the line broadening and from the line shift, respectively, using the Warren model [30]. Further quantities in (11.18) are the shear modulus of austenite in the fault plane (G_{111}) and the lattice parameter (a_0). $K_{111}\omega_0$ is a proportionality factor describing the relationship between the microstrain and the dislocation density, the dislocation character and the dislocation interaction [99]. This approach is commonly employed [101–103] despite the problems with the determination of the proportionality factor $K_{111}\omega_0$.

An alternative method for the SFE determination using XRD [104] is based on the proportionality between the SFE and the critical shear stress component (τ_{zx}),

$$\gamma_{\text{SF}} = \frac{\tau_{zx} b_p}{2}, \tag{11.19}$$

that is valid for the formation of very wide stacking faults, [cf. (11.6)]. $b_p = a_0|\langle 211\rangle|/6$ is the magnitude of the Burgers vector of the partial dislocations. According to Copley and Byun [9, 10], the separation distance between partial dislocations follows from the balance of the forces that act on the partial dislocations terminating a stacking fault, and is given by:

$$d_s = \frac{1}{8\pi} \cdot \frac{2-3\nu}{1-\nu} \cdot \frac{G b_p^2}{\gamma_{\text{SF}} - \frac{\tau_{zx} b_p}{2}}, \tag{11.20}$$

see also (11.5). In (11.20), ν is the Poisson ratio and G the shear modulus. If the distance between the partials becomes 'infinite', the work resulting from the impact of the shear stress component τ_{zx} on the partials must be in equilibrium with the stacking fault energy as described by (11.19). In the XRD approach from [104], the shear stress τ_{zx} is calculated from a (uniaxial) internal stress σ_x, which is needed to produce 'infinitely' wide SFs, and from the mean Schmid factor (M) that corresponds to the respective deformation state

$$\tau_{zx} = M\sigma_x. \tag{11.21}$$

The stress σ_x is proportional to the 'residual' elastic lattice deformation, which remains in the austenite after the plastic deformation. If the applied load is uniaxial and if the lattice deformation is measured in a direction perpendicular to this load [105], then the proportionality between stress and deformation is described by

$$\varepsilon_z^{hkl} \equiv \frac{d_z^{hkl} - d_0}{d_0} = s_1^{hkl}\sigma_x, \tag{11.22}$$

where $s_1^{hkl} = -\nu^{hkl}/E^{hkl}$ is the X-ray elastic constant (XEC) of austenite. The indices *hkl* emphasize the crystallographic anisotropy of the elastic constants. As for cubic materials, the interplanar distances can be converted directly to the lattice parameters,

$$\varepsilon^{hkl} \equiv \left\langle \frac{d^{hkl} - d_0}{d_0} \right\rangle = \left\langle \frac{a^{hkl} - a_0}{a_0} \right\rangle, \tag{11.23}$$

the internal stress in *fcc* austenite can be determined from the measured lattice parameters a^{hkl}. However, as the presence of the stacking faults leads to additional shift of the diffraction lines, [cf. (11.10)], the lattice parameter affected by the internal stress and stacking faults has the form of [104, 105]

$$a^{hkl} = a_0\left(1 + \sigma_x s_1^{100}\right) + 3a_0\left(s_1^{111} - s_1^{100}\right)\sigma_x \Gamma_{hkl}$$
$$+ \frac{\sqrt{3}}{4\pi}a_0\alpha G_{hkl}^{\text{SF}} - a_0 \cot\theta\,\Delta\theta \tag{11.24}$$

a_0 is the intrinsic lattice parameter of austenite (unaffected by internal stress and SFs), α the SF probability and $G_{hkl}^{\text{SF}} = \sum_{af} \pm(h + k + l)/\left[\left(h^2 + k^2 + l^2\right)m_{hkl}\right]$ the contrast factor of SFs from (11.10). In (11.24), the XEC s_1^{hkl} was replaced by

$$s_1^{hkl} = s_1^{100} + 3\Gamma_{hkl}\left(s_1^{111} - s_1^{100}\right), \tag{11.25}$$

where

$$\Gamma_{hkl} = \frac{h^2 k^2 + k^2 l^2 + l^2 h^2}{\left(h^2 + k^2 + l^2\right)^2} \tag{11.26}$$

is the cubic invariant describing the crystallographic anisotropy of XECs. The last term in (11.24) describes the correction of the measured lattice parameters for instrumental aberrations, which cause a line shift $\Delta\theta$. The fitting of measured lattice parameters with the function from (11.24) yields the intrinsic lattice parameter of austenite (a_0), the internal stress (σ_x) and the SF probability (α). Finally, the internal stress is used for calculation of the SFE:

$$\gamma_{\text{SF}} = \frac{\tau_{zx} b_p}{2} = \frac{1}{2}M\sigma_x \frac{a_0}{6}|\langle 211\rangle| = \frac{\sqrt{6}}{12}M\sigma_x a_0 \tag{11.27}$$

Another important method is the SFE calculation. Within the thermodynamic approach [23, 25, 106, 107], the SFE is calculated from the difference in the Gibbs energies of austenite and ε-martensite and from the strain and interface energies resulting from the faulting, see Sect. 11.2.3.1. The thermodynamic calculations are applied mainly to estimate the influence of certain alloying elements on the SFE. Nowadays, they are increasingly complemented by first-principles studies [24, 108].

However, if not based on experimental data, the modelled predictions often fail in giving reasonable trends, and show a systematic offset [107]. Therefore, the SFE calculations must be combined with experimental studies [92] or supported by other approaches like multivariate linear regression [109] or data driven machine-learning [110] in order to be verified.

11.4.3 *In Situ Diffraction Studies on TRIP/TWIP Steels During Plastic Deformation*

The capability of XRD methods to track the microstructure changes in TRIP/TWIP steels during their plastic deformation was tested on samples containing 3, 6 and 9 wt% Ni (PM X4CrMnNi16-7-3, X3CrMnNi16-7-6, PM X2CrMnNi16-7-9) that possess different SFEs and consequently different stabilities of metastable austenite. One part of the in situ XRD experiments was performed with a laboratory source under bending the samples in a four-point bending apparatus (Fig. 11.20). Advanced synchrotron XRD experiments were carried out at the PETRA III/DESY beamline P07 in Hamburg (Germany) in a deformation dilatometer.

During the XRD measurement in the four-point bending apparatus from Fig. 11.20, the total deformation force and the amount of the bending are measured in addition to the XRD patterns. These quantities are converted into the mechanical tensile stress σ_x^{mech} and into the strain in the outer fiber $\varepsilon_x^{\text{mech}}$ [105], respectively. The lattice parameters obtained from the line positions are plotted for selected deformation states as function of $3\Gamma_{hkl}$, cf. Fig. 11.21 and (11.24). In Fig. 11.21, the slope of the diagram is proportional to the internal stress σ_x, the departure of the lattice parameters from the linear dependence scales with the SF probability. As the measured line positions were corrected using an internal standard, the line shift in (11.24) was set to zero for fitting ($\Delta\theta = 0$).
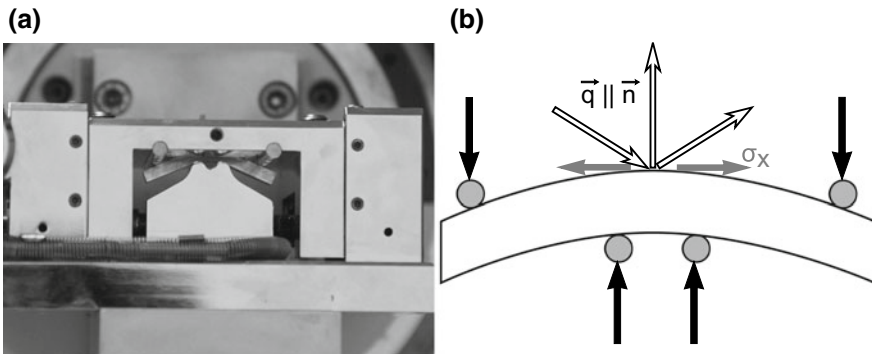
Fig. 11.20 Bending table used for the in situ XRD experiments (**a**). The beam path is shown schematically by the hollow arrows in (**b**)
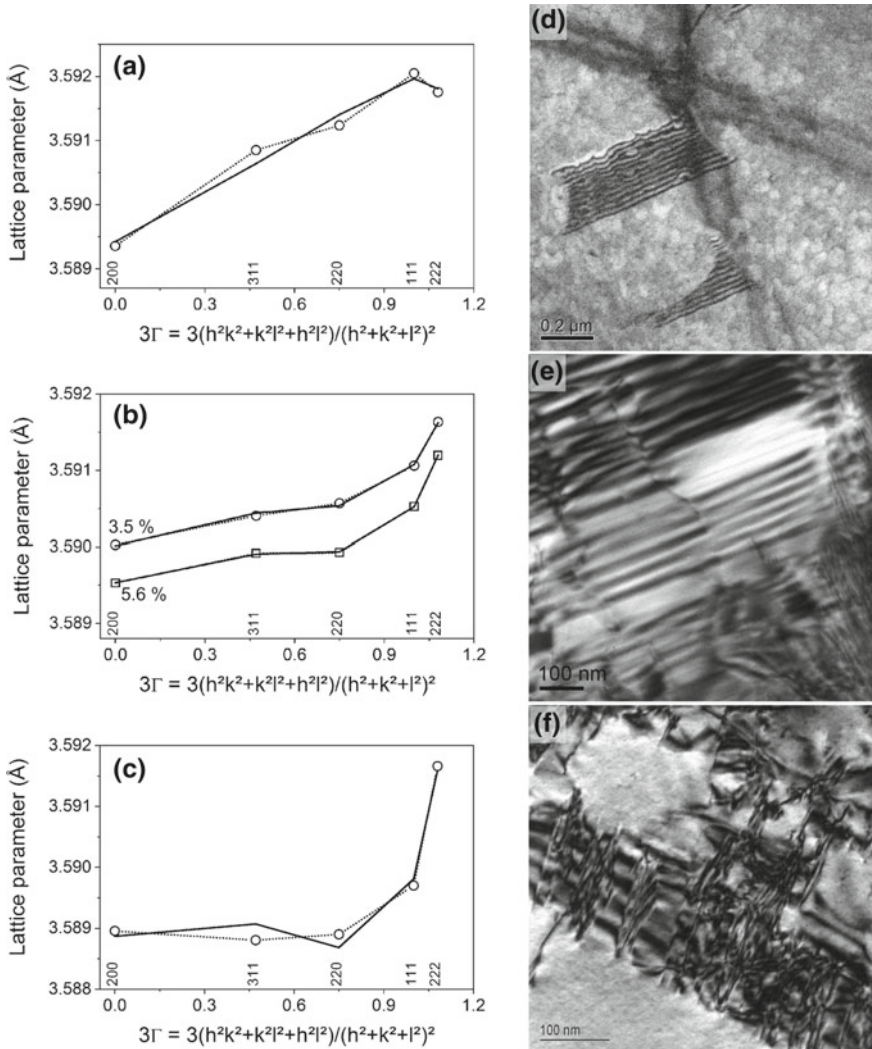
Fig. 11.21 Left-hand side: Lattice parameters of austenite deformed at the strains in the outer fiber of 1% (**a**), 3.5% and 5.6% (**b**), and 8.3% (**c**). Measured lattice parameters are plotted by interconnected open symbols, the lattice parameters fitted using (11.24) by solid lines. Corresponding TEM micrographs (**d**–**f**) at the right-hand side of the figure were taken in samples deformed to 0.5, 5 and 9%. Adopted from [104, 105]

The comparison of the measured lattice parameters with the lattice parameters fitted using (11.24) shows that the applied microstructure model is not valid for all deformation states (Fig. 11.21). While an excellent agreement between the measured and the calculated (fitted) lattice parameters was achieved for medium deformation states (Fig. 11.21b), the microstructure model cannot explain the anisotropy of the

lattice parameters observed at the lowest and highest deformations (Fig. 11.21a, c). The reason for the observed discrepancies is the invalidity of the Warren model for short (Fig. 11.21d) and crossing (Fig. 11.21f) stacking faults. Consequently, the application of this microstructure model to the measured lattice parameters can be used for verification of the presence of wide but non-intersecting SFs.

In Fig. 11.22, the lattice parameters a_0, the SF probabilities and the in-plane stresses (σ_x) are plotted against the strain in the outer fiber, and compared with the changes in the phase composition of the steel. As the intrinsic lattice parameter a_0 is supposed to stay constant during the deformation, its increase observed for $\varepsilon_x^{mech} < 2\%$ and $\varepsilon_x^{mech} > 6\%$ is another indicator of the invalidity of the Warren SF model. Analogously, the apparently negative SF probability observed for $\varepsilon_x^{mech} < 2\%$ is related to the early stage of the SF formation (cf. Fig. 11.21d). From the difference of the stress values σ_x, $\sigma_\parallel(311)$ and $\sigma_\parallel(222)$ in Fig. 11.22d, it can be supposed that the interaction of the local strain fields produced by partial dislocations in narrow SFs changes the crystallographic anisotropy of the SFs contrast factors. The SF crossing at larger deformations ($\varepsilon_x^{mech} > 6\%$, cf. Fig. 11.21f) leads to an apparent change of the crystallographic anisotropy of XECs, which can be seen on the difference
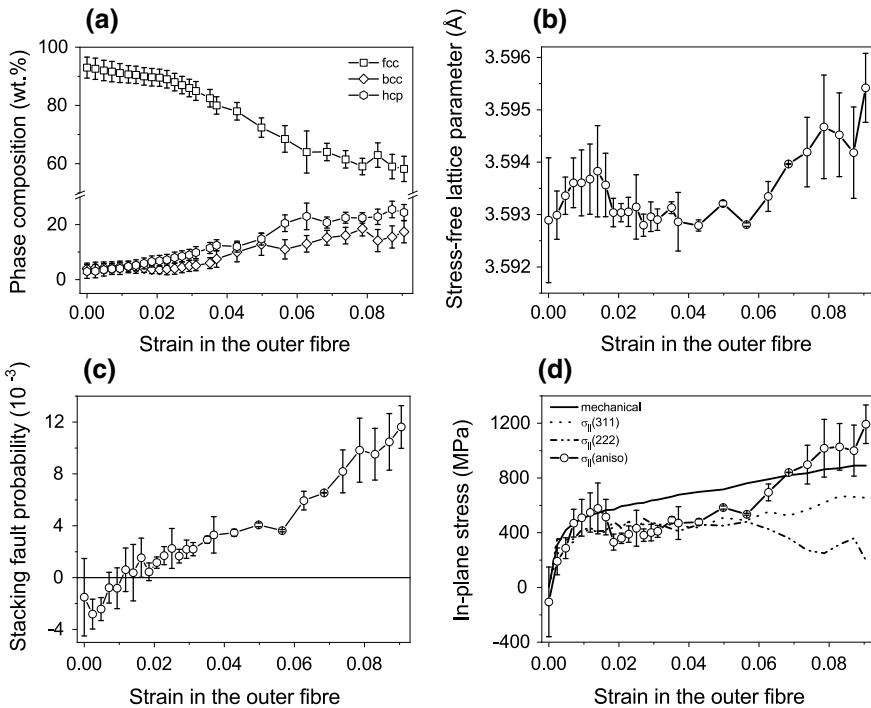
Fig. 11.22 Changes in the phase composition (**a**) and microstructure characteristics of the TRIP steel during plastic deformation. The lattice parameter a_0 (**b**), SF probability (**c**) and the internal stress in austenite σ_x (**d**) were obtained by fitting the measured lattice parameters according to (11.24)

between $\sigma_\parallel(311)$ and $\sigma_\parallel(222)$. These stresses were calculated directly from the lattice deformations measured in the respective crystallographic direction:

$$\sigma_\parallel(hkl) = \left(s_1^{hkl}\right)^{-1} \frac{d^{hkl} - d_0}{d_0} = \left(s_1^{hkl}\right)^{-1} \frac{a^{hkl} - a_0}{a_0} \qquad (11.28)$$

The XECs, $s_1^{311} = -1.60 \times 10^{-12}\,\text{Pa}^{-1}$, $s_1^{222} = s_1^{111} = -9.52 \times 10^{-13}\,\text{Pa}^{-1}$ and $s_1^{100} = s_1^{200} = -2.17 \times 10^{-12}\,\text{Pa}^{-1}$, were calculated using the Kröner approach [111] from the single-crystalline elastic constants of austenite, i.e., $C_{11} = 1.975 \times 10^{11}$, $C_{12} = 1.245 \times 10^{11}$ and $C_{44} = 1.220 \times 10^{11}$ Pa that were taken from the Landolt-Börnstein database [112].

The comparison of the SF densities (Fig. 11.22c) with the phase compositions (Fig. 11.22a) and the corresponding TEM micrographs (Fig. 11.21d–f) confirmed that up to $\varepsilon_x^{\text{mech}} \cong 2\%$, the deformation behavior of austenite is dominated by the formation and widening of SFs. For $\varepsilon_x^{\text{mech}}$ above 2%, the SF density increases, which leads to the local ordering of SFs that is recognized by XRD as the ε-martensite formation. At the deformations above 6%, the SFs form also on crystallographically equivalent lattice planes {111} and interact, which facilitates the formation of α'-martensite as explained in Sect. 11.3.

The validity range of the Warren model that was identified by the above routine was used for calculation of the SFE from the internal stress (σ_x, $\sigma_\parallel(311)$ or $\sigma_\parallel(222)$) and from the lattice parameter a_0 measured by XRD. For the SFE calculation, (11.27) was employed. As the change in the preferential orientation of crystallites was negligible in this deformation range, the Schmid factors were assumed constant (independent of the deformation state) and obtained from the EBSD measurements that were carried out on non-deformed samples. The SFEs determined using this method were 17.5 $\pm$ 1.4 mJ m^{-2} for the TRIP steel X3CrMnNi16-7-6 and 8.1 $\pm$ 0.9 mJ m^{-2} for the TRIP steel X4CrMnNi16-7-3 [104], and 24.1 $\pm$ 2.5 mJ m^{-2} for the TRIP steel X2CrMnNi16-7-9.

For a comprehensive description of the microstructure development during plastic deformation, the TRIP/TWIP steels PM X4CrMnNi16-7-3, X3CrMnNi16-7-6 and PM X2CrMnNi16-7-9 containing 3, 6 and 9 wt% Ni, respectively, were investigated using in situ synchrotron diffraction during compression [113]. In the non-deformed state, the samples had cylindrical shape ($\varnothing$ 4 mm × 8 mm), and were fully austenitic and fine-grained. The synchrotron diffraction experiments were carried out at beamline P07 of PETRA III at DESY (Hamburg, Germany). The high energy and the short wavelength of the synchrotron radiation (100 keV, $\lambda = 0.1235$ Å) enabled measurements in transmission diffraction geometry, which is more appropriate for explanation of the bulk materials properties than the surface-sensitive laboratory XRD studies [114]. Furthermore, the short wavelength of the synchrotron radiation provided a broad coverage of the reciprocal space up to

$$q = \frac{2\pi}{d} = \frac{4\pi \sin\theta}{\lambda} = 8.87\,\text{Å}^{-1}, \qquad (11.29)$$

which is beneficial for measurements in a broad range of the diffraction indices *hkl*, especially in materials with relatively small elementary cell. For austenite, nine diffraction peaks were recorded (up to 422). In (11.29), q is the maximum magnitude of the diffraction vector and d the minimum interplanar spacing that are accessible at the maximum diffraction angle $2\theta = 10°$ and at the wavelength of 0.1235 Å. High flux of the synchrotron beam enables real in situ measurements. Relaxation effects in the sample during the acquisition of the individual diffraction patterns (measuring time about 1 s) are almost eliminated.

The samples were deformed in a deformation dilatometer (BÄHR DIL 850) until the maximum force, corresponding to a technical stress of 1590 MPa. The in situ compression was carried out in 35 quasi-static discrete load steps. The holding time between the deformation steps (approx. 1 s) resulted from the time that was needed for recording the diffraction patterns. The load direction was perpendicular to the direction of the primary synchrotron beam (Fig. 11.23). In this diffraction geometry, the angle Ψ between the load direction and the diffraction vector varies between $2\theta/2$ and $90°$ along the Debye rings. The continuous change of the angle Ψ allows the determination of internal stresses and preferred orientations of crystallites in all present phases from a single 2D diffraction pattern.

For the analysis of the 2D diffraction patterns, the recorded images were integrated in $5°$ wide sections along the Debye rings in order to conserve the Ψ-dependent information. The 72 diffraction patterns (diffracted intensities versus diffraction angles for individual Ψ sections, see Fig. 11.24) were subjected to a coupled Rietveld refinement using MAUD [115, 116]. The microstructure models employed for the Rietveld refinement of individual diffraction patterns included: (i) anisotropic line broadening from perfect dislocations according to the Popa model [88], (ii) anisotropic line
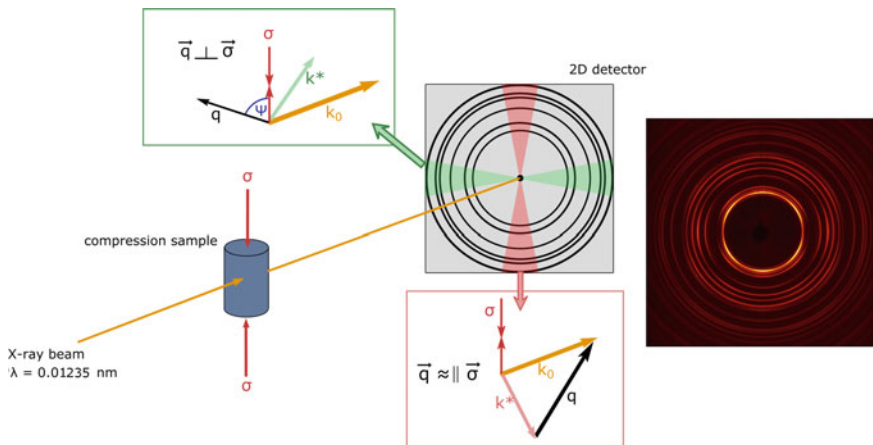

Fig. 11.23 Setup of the in situ compression tests in transmission geometry. The sketches in the green and red boxes show the alignment of the diffraction vector that is perpendicular and nearly parallel to the load direction in the correspondingly colored segments of the 2D diffraction pattern. On the right-hand side of the panel, a single 2D diffraction pattern is shown

Fig. 11.24 The 1D diffraction patterns integrated over 5° wide segments of the 2D diffraction pattern from Fig. 11.23
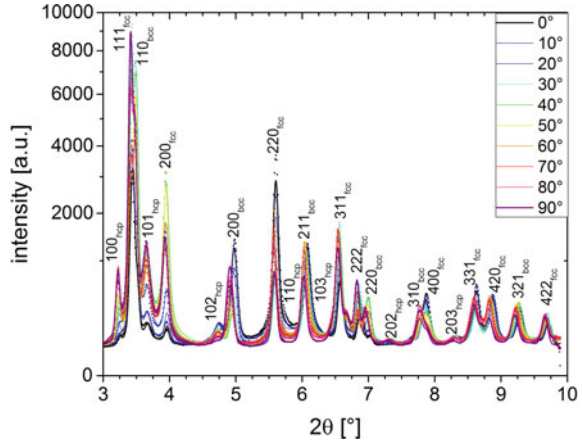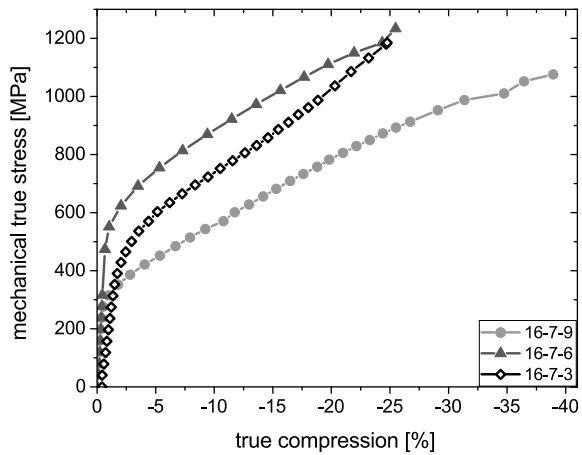

Fig. 11.25 True stress—true strain curves measured during the compressive deformation of the 16Cr-7Mn-xNi steels. Adopted from [113]

broadening and anisotropic line shift caused by SFs according to the Warren model [30] and (iii) anisotropic line shift caused by anisotropic elastic lattice deformation according to the Moment Pole Stress model [117]. In the Moment Pole Stress model, only the stress component σ_{33} was considered. The same elastic constants of the austenite were used like for the in situ XRD experiments during bending. Fractions of individual phases were determined after the diffracted intensities have been corrected for preferred orientations of crystallites using the Ψ dependence of the diffracted intensities [115, 118], because the texture correction improves significantly the reliability of the quantitative phase analysis [119].

Mechanical behavior of the Cr–Mn–Ni 16-7-x TRIP/TWIP steel samples during the compressive load is depicted in Fig. 11.25. The deformation and the applied force were measured by the dilatometer and converted to true stress and true strain. The material with the highest SFE (24.1 mJ/m^2) and with the highest Ni content

(9%) exhibits the lowest stress level and a nearly constant strain hardening. This kind of strain hardening is commonly associated with the TWIP effect [120]. The sample with the lowest SFE (8.5 mJ/m^2) and lowest Ni content (3%) possesses the most pronounced strain hardening, which results in a sigmoidal flow curve that is characteristic for intense martensitic transformation [121]. In the sample containing 3 wt% Ni, the formation of ε-martensite begins at ca. 1% compression.

The maximum amount of ε-martensite (about 19 vol%) is reached at 20% deformation (Fig. 11.26). The α'-martensite forms at relatively low deformations. At the deformation of 15%, it becomes the dominant martensitic phase, which grows at the expense of austenite and ε-martensite at deformations exceeding 20%. In sample X2CrMnNi16-7-9, the formation of ε-martensite is delayed and the α'-martensite does not form up to a 40% compression. This dependence of the martensites formation on the Ni content is a result of a lower driving force for the martensitic transformation in materials with higher SFE that was discussed in Sects. 11.2.3 and 11.3. The sample containing 6% Ni (SFE = 17.5 mJ/m^2) shows almost constant strain hardening like the steel X2CrMnNi16-7-9, while the development of the phase composition resembles the TRIP steel with 3 wt% Ni. However, the stress level in sample X3CrMnNi16-7-6 measured beyond the onset of the plastic deformation is clearly too high. The results of the diffraction analysis (see below) support the assumption that the high stress level is related to an incompletely recrystallized initial microstructure.

The σ_{33} component of the internal stress in austenite, which is parallel to the applied compression, increases during the sample compression (Fig. 11.27a), but is constantly lower than applied mechanical stress (cf. Fig. 11.25). The increase of σ_{33} indicates the strain hardening that is caused by the increase of dislocation density and thus by the increase of dislocation-induced microstrain (Fig. 11.28), and by the interaction of dislocations in austenite with the newly formed martensites [113].

The interplay of these effects can be illustrated on the lowest internal stress (Figs. 11.24 and 11.27a), lowest microstrain (Fig. 11.28) and delayed martensite

Fig. 11.26 Phase fractions of *fcc* austenite, *hcp* ε-martensite and *bcc* α'-martensite during the deformation of the samples. Adopted from [113]
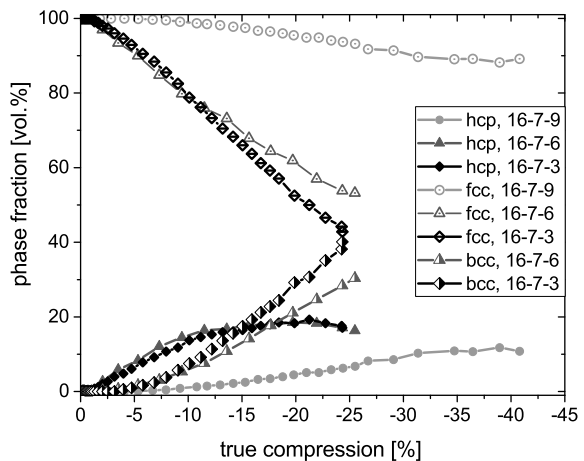
Fig. 11.27 a Internal elastic lattice stress in austenite in the compression direction, obtained from the in situ synchrotron diffraction. **b** Difference between the (total) mechanical true stress from Fig. 11.25 and the lattice stress, adopted from [113]
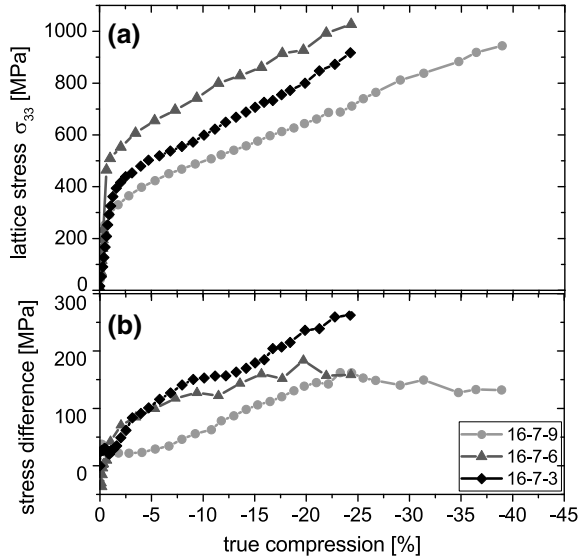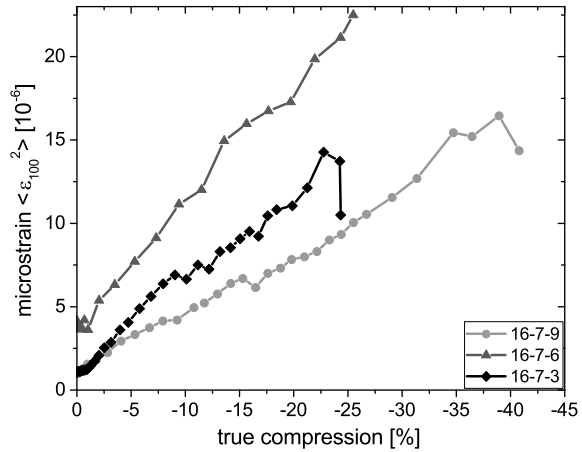
Fig. 11.28 Squared microstrain—a quantity proportional to the dislocation density

formation (Fig. 11.26) in sample X2CrMnNi16-7-9. Weaker defect formation and retarded martensitic phase transformation are also the reasons for the smallest difference between the applied mechanical stress and internal (elastic) lattice stress in sample X2CrMnNi16-7-9 (Fig. 11.27b).

The largest difference between the mechanical stress and σ_{33} observed in sample X4CrMnNi16-7-3 for deformations beyond 7.5% suggests that newly formed martensites carry a significant part of the external load. In this deformation range, the amount of α'-martensite increases most quickly in the steel with lowest Ni content (sample X4CrMnNi16-7-3 in Fig. 11.26).

Fig. 11.29 Evolution of the probability of isolated intrinsic stacking faults in austenite under compression
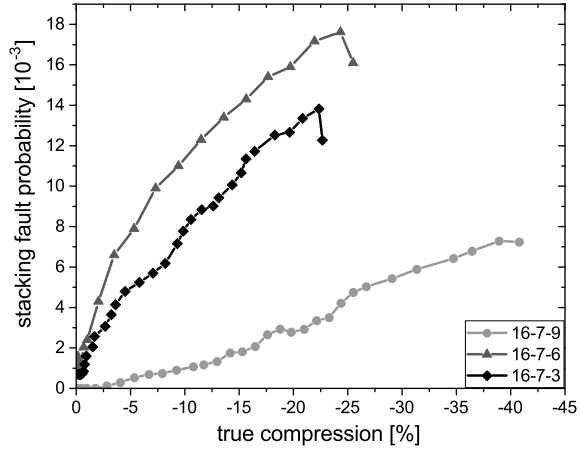
The stacking fault probabilities (SFPs, Fig. 11.29) correlate generally with the amount of ε-martensite (Fig. 11.26), because the ε-martensite is formed by the ordering of dense stacking faults, see Sect. 11.2. For this reason, both quantities are expected to increase with decreasing SFE. Still, at the lowest deformations, the SFs must be created before ε-martensite can form, thus the initial increase of SFP occurs always earlier, i.e., at lower strains than the onset of the ε-martensite formation. The steep increase of the SFP in samples X4CrMnNi16-7-3 and X3CrMnNi16-7-6 and the early onset of the ε-martensite formation indicate the dominant role of stacking faults as deformation mechanism. The unexpectedly high SFP in the deformed steel X3CrMnNi16-7-6 as compared with the SFP in the steel X3CrMnNi16-7-3 (Fig. 11.29) is caused by a higher density of dislocations in incompletely recrystallized initial sample X3CrMnNi16-7-6 (Fig. 11.28). The lowest SFPs were measured for the 9% Ni steel, because this steel possesses the highest SFE. Especially in this steel, the onset of the SF formation is slightly delayed (shifted to higher strains), because the initial deformation is realized by dislocation slip. Because of its higher SFE, the formation of twins is expected in this steel, but the presence of the twins cannot be evidenced easily from the diffraction data.

Although the formation of SFs and the martensitic transformations are the dominant deformation mechanisms in the TRIP steels, the role of perfect dislocations is not neglectable, because the perfect dislocations are the precursors of partial dislocations, SFs and ε-martensite (or twins in TWIP steels). In order to visualize the development of the dislocation density in the TRIP/TWIP steels during their plastic deformation, the squared microstrain $\langle \varepsilon_{100}^2 \rangle$ was plotted as a function of the true compression in Fig. 11.28. According to Wilkens [122], the squared microstrain is proportional to the dislocation density [cf. (11.15)]

$$\langle \varepsilon_{hkl}^2 \rangle = \frac{\pi}{8} M^2 \rho b^2 \bar{C}_{hkl}, \tag{11.30}$$

and can be determined directly from the dependence of the diffraction line broadening on the magnitude of the diffraction vector ($|\vec{q}| = 2\pi d^*_{hkl}$):

$$\beta_{hkl} = \frac{K}{D} + \beta^{\text{SF}}_{hkl} + 2\sqrt{\langle \varepsilon^2_{hkl}\rangle} \cdot d^*_{hkl}. \tag{11.31}$$

Additional contributions to the measured line broadening stem from the (small) crystallite size (K/D) and from stacking faults (β^{SF}_{hkl}), [cf. (11.14)].

In the steels containing 3 and 6% Ni, the dislocation-induced microstrain increases steeply during initial straining (Fig. 11.28). The offset of both curves is caused by the incompletely recrystallized initial microstructure of sample X3CrMnNi16-7-6 that contained a higher dislocation density. The higher dislocation density persists throughout the whole deformation process, and accounts for the higher SFP, higher lattice stress level and more intense ε-martensite formation in this sample. While the squared microstrain in steel X3CrMnNi16-7-6 increases almost linearly with increasing deformation, in the steel with a lower Ni concentration (X4CrMnNi16-7-3) the increase of the squared microstrain is reduced after ca. 9% compression, due to an intense stacking fault formation and martensitic transformation. The squared microstrain in the steel X2CrMnNi16-7-9 increases also almost linearly, but its increase is slower than in the steel X3CrMnNi16-7-6.

The comparison of the evolution of the dislocation-induced microstrain in the three steels under study suggests that the dislocation density and consequently the expected contribution of the dislocation slip to the plastic deformation decreases with decreasing SFE. Other deformation mechanisms such as the formation of stacking faults and phase transformations become dominant [113]. This change in the dominant deformation mechanism goes along with the transition from the TWIP to the TRIP behavior, and can be substantiated by microscopic studies using, e.g., ECCI and EBSD.

The ECCI and EBSD micrographs of the TRIP/TWIP steels deformed up to the maximum compression depicted in Fig. 11.30 show dislocation arrangements, stacking faults, deformation bands and α'-martensite nuclei. The characteristic microstructure features of the 3% Ni steel are pronounced deformation bands existing on several slip planes, single stacking faults and regions transformed to α'-martensite (Fig. 11.30a). The 6% Ni steel (Fig. 11.30b) exhibits similar features, which are finer scaled because of the incompletely recrystallized initial microstructure. Distinct dislocation structures and their mutual interactions can be seen in deformed steel X2CrMnNi16-7-9 (Fig. 11.30c), where some deformation bands become curved due to their intense interaction with the dislocation arrangements. As twins in austenite are hardly to be distinguished from ε-martensite using ECCI (see Sect. 11.4.1), the nature of the deformation bands and the relative density of the stacking faults within the bands were investigated by EBSD in the 9% Ni steel (Fig. 11.30d).
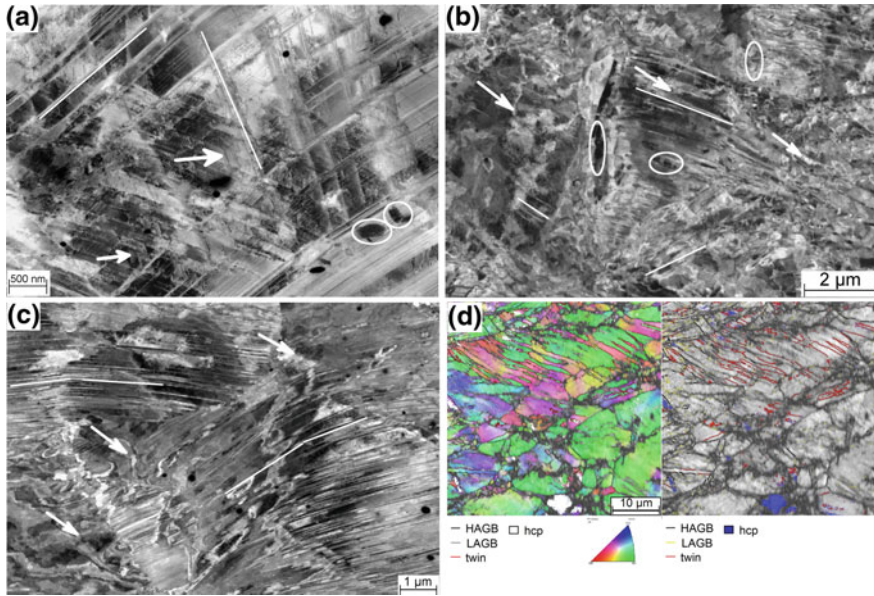
Fig. 11.30 SEM microstructure characterization of deformed samples after the respective maximum compression. **a** ECC image of the 3% Ni steel showing deformation bands (lines), single stacking faults (arrows) and α'-martensite nuclei (circles). **b** ECC image of the highly defective microstructure in the 6% Ni steel showing deformation bands (lines), dislocation arrangements (arrows) and α'-martensite nuclei (circles). **c** Curved deformation bands (lines) and dislocation structures (arrows) in the 9% Ni sample. **d** EBSD maps of this sample, at the left: grain orientation and grain boundaries, especially twins (red lines), as well as local occurrence of *hcp* ε-martensite (white); at the right: mapping of the same area, grain and twin boundaries are plotted together with the band contrast (gray)

11.5 Interplay of Deformation Mechanisms, Development of Deformation Microstructure

11.5.1 Interaction of Microstructure Defects in Deformation Bands

The formation of deformation bands plays a central role in the strain hardening of austenitic steels. As discussed above, the deformation bands accommodate dense SFs that serve as precursors of martensitic phase transformations and twinning in austenite. From the micromechanical point of view, the deformation bands produce strain fields, which interact with the microstructure defects existing outside of the deformation bands. This interaction is illustrated by the TEM image shown in Fig. 11.31, where a deformation band formed on the primary slip system acts as an obstacle for the motion of SFs and for the dislocation slip on the secondary slip systems. The interaction between the primary deformation band and the dislocations gliding on the

Fig. 11.31 TEM micrograph evidencing the obstacle effect of a deformation band for the dislocation motion on secondary slip systems. Adopted from [34]
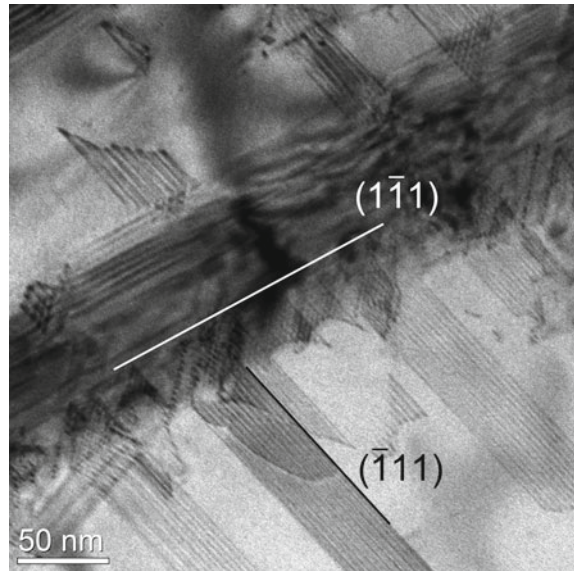

secondary slip systems reduces the mean free path length of the dislocations [120, 123, 124], which is a phenomenon that is known as dynamic Hall-Petch effect.

A secondary stacking fault impinging a twin or deformation band must constrict, which means that the partial dislocations of the SF must recombine in order to be able to react with the stacking fault arrangement. Such a dislocation reaction is energetically unfavorable, and can only occur under a local stress concentration [125]. The interactions between deformation bands and other microstructure defects are illustrated exemplarily in Fig. 11.31, where the secondary stacking faults $(\bar{1}11)$ that are stopped at the deformation band on the $(1\bar{1}1)$ plane seem to constrict partially, but a straight intersection of SFs located on the primary slip system by the SFs located on the secondary slip system is not observed.

Furthermore, the presence of the deformation bands inhibits the annihilation of nearly perfect dislocations having opposite Burgers vectors, as these dislocations are simply separated from each other. The annihilation of dislocations is additionally obstructed by their reduced cross-slip. The deformation bands also impede an arrangement of the dislocations in lower-energetic cell structures. Hence, the presence of deformation bands suppresses the dynamic recovery and enhances the dislocation storage capacity of the material. Dislocations accumulate in the interspace between the deformation bands much more than in materials without planar defects. This finding is confirmed by the continuous increase of the dislocation-induced microstrain measured by XRD in compressed steel PM X5CrMnNi16-6-9 (Fig. 11.32). The simultaneously increasing SF probability indicates that the stacking faults form during the whole deformation process, also on secondary slip systems, contribute continuously to a refinement of the microstructure, and thus maintain a high strain-hardening rate by reducing the mean free paths of gliding dislocations.

Fig. 11.32 Trends of squared microstrain and SF probability for a deformed PM X5CrMnNi16-6-9 steel evidencing the reduced recovery and resulting high dislocation density [34]
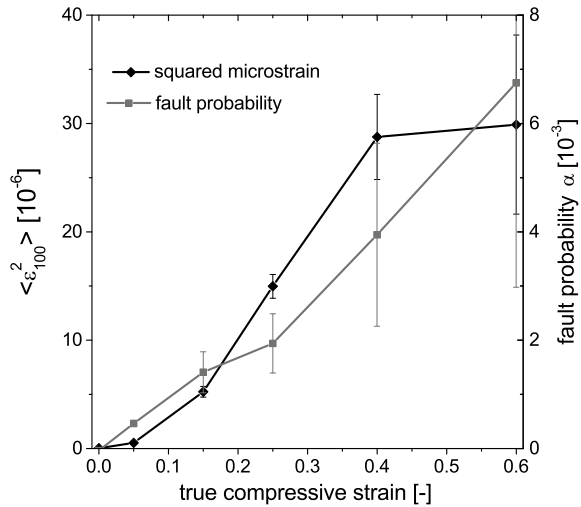
The interactions of microstructure defects discussed above can be found in deformation bands containing isolated SFs and concentrated SFs in form of ε-martensite and twins in austenite. Nevertheless, the extent of the interaction increases with the SF density, thus it is superior for imperfect twins. Correspondingly, enhanced strain hardening was reported for the TWIP steels showing no martensitic transformation [12, 120, 126].

If α'-martensite forms within the deformation bands, even enhanced strengthening is observed. The dislocation glide within the deformation bands is additionally obstructed by the newly formed phase boundaries. The mechanisms of the deformation band formation and the strengthening by the α'-martensite nucleation are summarized in Fig. 11.33.

During plastic deformation, the equilibrium dissociation width of beneficially oriented partial dislocations in austenite (1) is increased by external applied shear stress (2). New dislocations are generated and the deformation band forms (3), which is accompanied by conventional cold work strengthening. Formation of SFs and deformation bands on the secondary slip systems produces local strain fields that facilitate the nucleation of α'-martensite (4) having a specific volume of about 2.5% larger than austenite. The α'-martensite boundaries and the lattice strains resulting from the volume expansion are hard obstacles for the dislocation motion. They pin existing SFs, thus the further plastic deformation produces new (perfect) dislocations alongside the existing deformation band and leads to their dissociation (5). This explains the observed lateral growth of the deformation bands [40] and the high volume fraction of the ε-martensite of ≤ 25 vol% (Figs. 11.18 and 11.26) at moderate stages of straining.
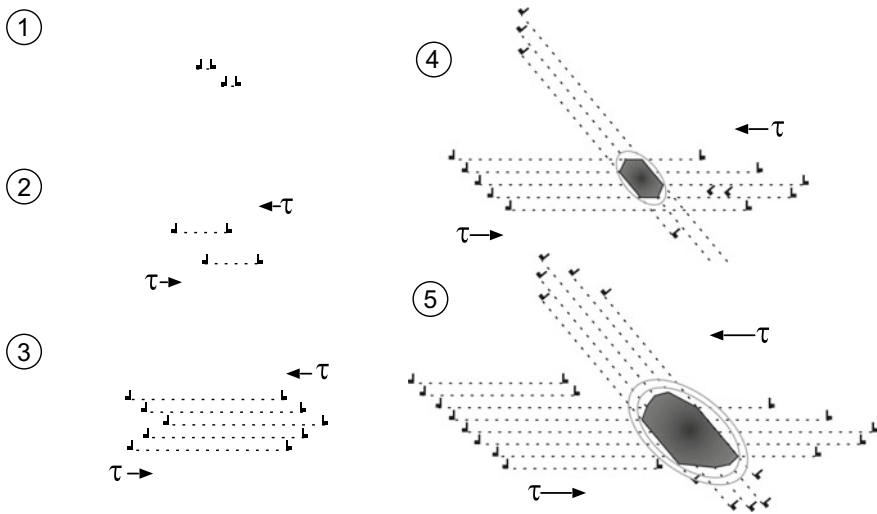
Fig. 11.33 The interplay of the deformation band formation and the α'-martensite nucleation contributes additionally to the strain hardening in austenite. Adopted from [61]

11.5.2 Orientation Dependence of the Stacking Fault and Deformation Band Formation

A complex, heterogeneous microstructure is observed in deformed austenitic steels, even if they consist of equiaxed grains with unimodal grain-size distribution. As shown in the ECCI micrograph in Fig. 11.34, in some grains the stacking faults and deformation bands dominate, whereas other grains are free of planar defects and exhibit dislocation structures instead.

These differences in the deformation behavior can be explained by the orientation dependence of the stacking fault and deformation band formation, which follows from the dependence of the difference between the Schmid factors of the leading and trailing partials on the individual grain orientation (Fig. 11.35a). These partial dislocations experience different shear stresses, which depends on the orientation of their Burgers vector with respect to the direction of the external load [9]. From Fig. 11.35a, it can be concluded that the grains oriented with their ⟨001⟩ direction nearly parallel to the applied compression should have the highest tendency to the stacking fault formation. In these grains, the leading partial dislocation has a clearly higher Schmid factor than the trailing one, thus the SFs are widened upon compression. For the grain orientations with a negative Schmid factor difference (Fig. 11.35a), the trailing partial dislocations move faster than the leading ones, thus the stacking fault is closed.

For the grains with negative difference of the Schmid factors of leading and trailing partial dislocation, this trend was confirmed by EBSD measurements, which revealed
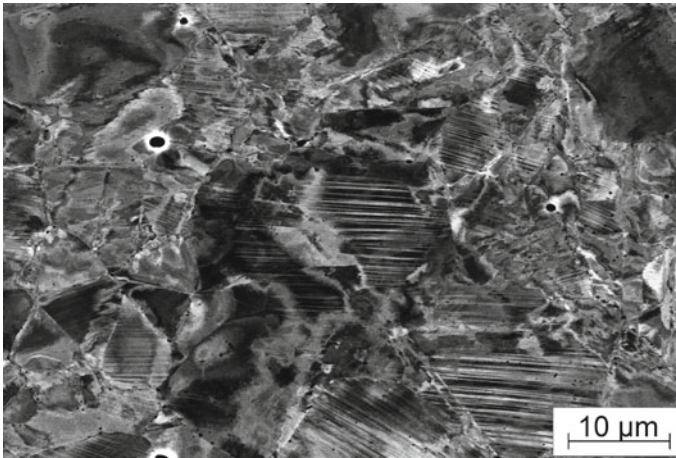
Fig. 11.34 Electron channeling contrast (ECC) image of the heterogeneous microstructure in a 15% strained PM X5CrMnNi16-6-9 steel. Adopted from [34]

that grains with the orientations between ⟨101⟩ and ⟨111⟩ along the deformation direction were almost free of deformation bands (Fig. 11.35c, e). In Fig. 11.35c, these grains are highlighted. Figure 11.35e shows their orientation density distribution. The highest density of SFs and deformation bands should be observed for grain orientations with positive Schmid factor difference (Fig. 11.35a). However, this expectation was not confirmed experimentally, as the ECCI/EBSD measurement (Fig. 11.35d, f) revealed that the grains with the highest density of SFs and deformation bands have orientations between ⟨102⟩ and ⟨113⟩ with respect to the compression direction. The reason for this apparent discrepancy is that the dissociation of perfect dislocations must be preceded by their formation that is activated according to the Schmid factor from Fig. 11.35b. After the initiation of faulting, the grain orientation can still be rotated by dislocation slip (on secondary slip systems), producing the typical formation of a ⟨101⟩ compression texture in *fcc* materials. This results in the observation of Fig. 11.35f that faulted grains are not sharply clustered around ⟨001⟩, but rather found between ⟨102⟩ and ⟨113⟩ orientations. The grains without stacking faults are oriented according to the ⟨101⟩ fiber texture in compressive load direction.

Consequently, the orientation dependence of the stacking fault and deformation band formation in austenite is controlled by the Schmid factors of perfect dislocations and SFs, because the plastic deformation of austenite is activated by the formation of perfect dislocation and their dissociation. For compression, the interplay of these mechanisms favors the SF formation on the primary slip system for orientations between ⟨102⟩, ⟨113⟩ and ⟨001⟩, while the formation of the deformation bands is delayed in grains having the orientations between ⟨101⟩, ⟨111⟩, ⟨113⟩ and ⟨102⟩. For tensile deformation, the favorable and unfavorable grain orientations are exchanged, because the sign of the Schmid factors of the partials switches with the inversion of the load direction.
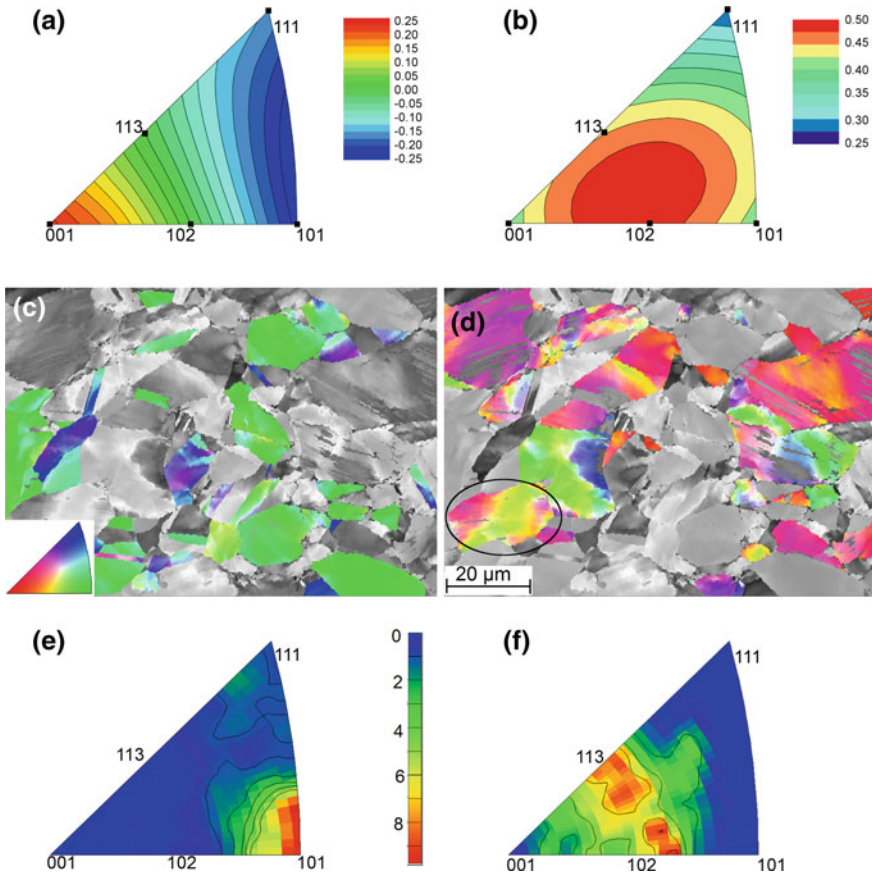
Fig. 11.35 Orientation dependence of the stacking fault and deformation band formation after 15% compression. In panel (**a**), the difference between the Schmid factors of leading and trailing partial for compression is presented. In panel (**b**), the orientation dependence of the Schmid factor for perfect dislocations on the primary slip system is plotted. EBSD maps show the orientation of grains that are almost free of deformation bands (**c**) and that accommodate pronounced deformation bands (**d**). The grey scale values in panels (**c**) and (**d**) are related to the EBSD band contrast. The corresponding inverse pole figures shown in panels (**e**) and (**f**) depict the orientation density distribution of the respective grains. Adopted from [34]

11.5.3   Dependence of the Deformation Mechanisms on Local Chemical Composition and Temperature

The dependence of the stacking fault and deformation band formation on the local orientation of the austenite grains is no exclusive reason for the existence of complex heterogeneous microstructures that are typically observed in deformed austenitic steels. In general, the prevailing deformation mechanism in these steels depends on the SFE of austenite, which is, from the thermodynamic point of view, a function

of the difference between the Gibbs energy of austenite and the Gibbs energy of ε-martensite (Sect. 11.2.3.1). As the difference of the Gibbs energies depends on the chemical composition of the steel, the deformation mechanisms are strongly influenced by the concentrations of the alloying elements. This is not only true on the macroscopic scale, where the SFE is generally affected by the overall chemical composition of the TRIP/TWIP steels (Sect. 11.4.3), but also on the microscopic scale, where local concentration fluctuations lead to a coexistence of deformation mechanisms even within individual grains [127].

Another result of the thermodynamic consideration of SFE is that the stacking fault energy increases with increasing temperature (through the temperature dependence of the Gibbs energies). The corresponding dependence of the deformation mechanisms on the temperature is illustrated in Fig. 11.36 for the steel composition X3CrMnNi16-6-6. From the XRD patterns, it can be seen that at the end of the uniform elongation the amount of the martensitic transformation decreases with increasing deformation temperature. As discussed in Sects. 11.2 and 11.3, both martensites (ε and α') occur in deformation bands, which accommodate a high density of (ordered) SFs. With decreasing deformation temperature, the SFE decreases, which facilitates the formation of extended SFs and the transformation of austenite to ε- and α'-martensites. The sample deformed at $-60\,°C$ contains mainly α'-martensite. At higher temperatures (above room temperature), the increase of SFE with increasing deformation temperature hinders the SF formation. Above approx. 60 °C, the deformed steel X3CrMnNi16-6-6 consists predominantly of austenite. The diffraction peaks corresponding to the *bcc* phase that were observed above 100 °C stem from initial δ-ferrite,

Fig. 11.36 XRD patterns after mechanical straining of cast TRIP steel samples at different testing temperatures until the end of uniform elongation (see right column of Fig. 11.37), indicating different amounts of martensitic transformation and remaining austenite [4]
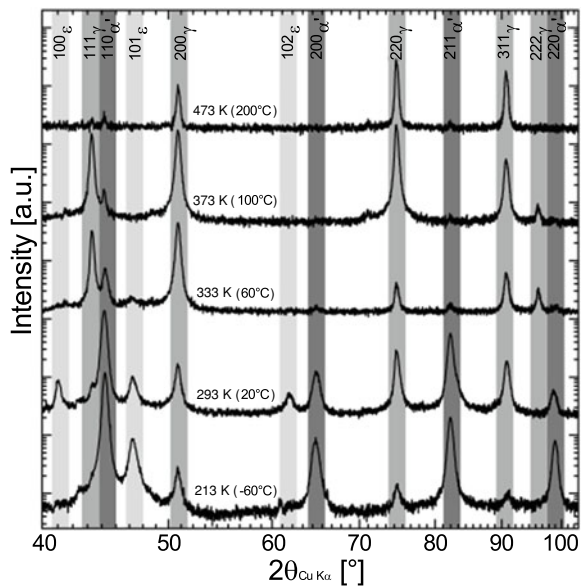
which is also present in small fractions from the primary ferritic solidification of the cast material.

The results of XRD phase analysis were complemented by the SEM/EBSD experiments (Fig. 11.37), which helped in visualization of the microstructure defects and their arrangement that are related to the change in the phase composition of the deformed samples.

It was confirmed that the martensites, which form at the deformation temperatures below 60 °C, grow first inside and later out of the (former) deformation bands (Fig. 11.37a, b, f and g). At deformation temperatures above 60 °C, the martensite formation is reduced, while the twinning of austenite and the formation and slip of perfect dislocations become the most important mechanisms of the plastic deformation (Fig. 11.37c, d, e, h, i and j). At the deformation temperature of 60 °C, all microstructure features, i.e., α'-martensite, SFs, ε-martensite and twins in austenite are present (Fig. 11.37c, h), which means that the deformation mechanisms facilitated by the formation of the respective microstructure feature coexist. At the deformation temperatures above 60 °C, the density of twins in austenite increases rapidly (Fig. 11.37d, i). As the twins act as obstacles for dislocation glide, the perfect dislocations are concentrated in the areas between the deformation bands consisting of twins (Fig. 11.37d, e). At 200 °C, twins are only scarcely observed and dislocation configurations indicate that the deformation was essentially carried by perfect dislocation slip (Fig. 11.37e, j).

The temperature dependence of the deformation mechanisms discussed above is depicted schematically in Fig. 11.38. The link between the deformation temperature and SFE (γ_{SF}) emphasizes that the deformation mechanisms are essentially controlled by the stacking fault energy. The SFE at room temperature was determined experimentally (Sect. 11.4.3). The increase of SFE with increasing temperature was calculated from the change of $\Delta G^{\gamma \to \varepsilon}$ with temperature (Sect. 11.2.3.1).

The dislocation-induced plasticity is the fundamental deformation mechanism, thus its occurrence is highlighted by a grey hachure in the entire temperature range. At room temperature, the perfect dislocations dissociate quickly upon deformation, and form stacking faults. The stacking faults concentrate in deformation bands and form ε-martensite, below the critical temperature (M_D) also α'-martensite. Below the martensite start temperature (M_s), the formation of α'-martensite is further accelerated even without deformation. A high volume of α'-martensite at low (deformation) temperatures is one of the reasons for a high ultimate tensile stress (UTS in Fig. 11.38). Another reason for the increase of UTS with decreasing deformation temperature is the reduction of the mean free path of dislocations in the deformation bands by the successive nucleation of α'-martensite crystallites (cf. Sect. 11.5.1).

In contrast to UTS, which decreases monotonously with increasing deformation temperature, the uniform elongation (UE) shows pronounced maximum between room temperature and 150 °C, which corresponds to the SFE range between 15 and 34 mJ/m^2. In this temperature/SFE range, an intensified formation of ε-martensite and twins was observed that was already reported for various austenitic stainless steels in literature [59, 128]. The high amount of local shear approaching $0.35 \left(\cong \sqrt{2}/4 \right)$ and
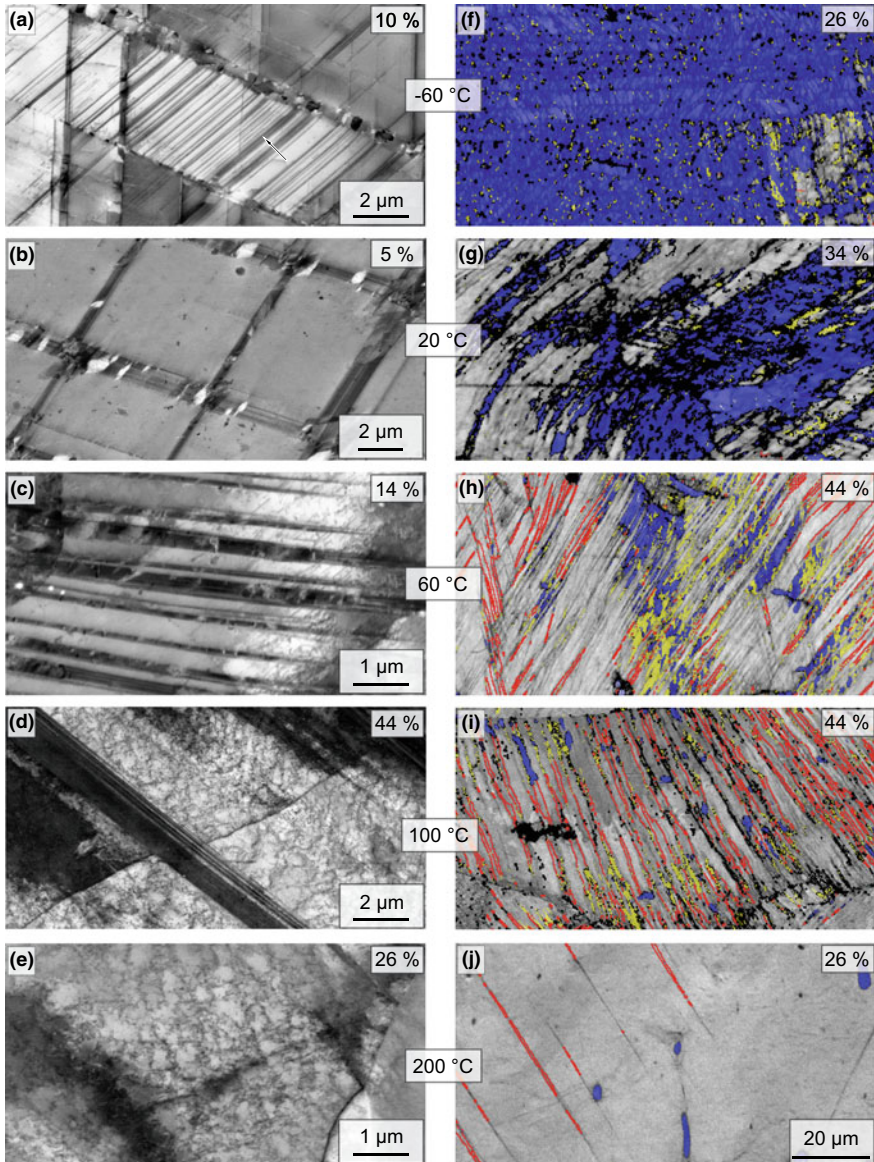
Fig. 11.37 Micrographs of coarse-grained TRIP/TWIP steel samples deformed at different strains at various testing temperatures. Left column: inverted ECCI images showing the deformation microstructures. Right column: EBSD phase maps highlighting austenite (the grey scale corresponds to the band contrast), ε-martensite (in yellow), α'-martensite (in blue) and not indexed regions (in black). The red lines mark the $\Sigma3$ boundaries between deformation twins. All EBSD maps share the same scale bar. According to [4]
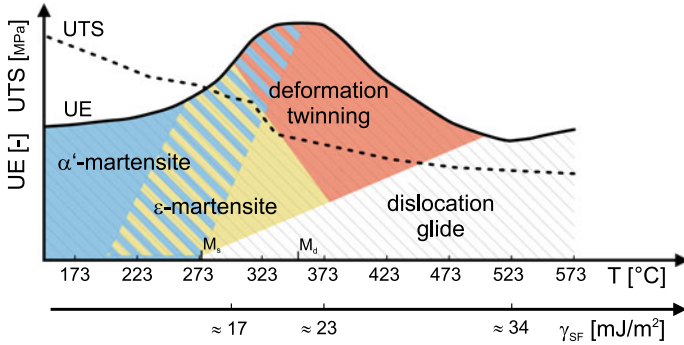
Fig. 11.38 Schematic representation of temperature dependence of the active deformation mechanisms in the X3 CrMnNi16-6-6 steel and their influence on ultimate elongation (UE) and ultimate tensile strength (UTS) [4]. The relationship between temperature and SFE (γ_{SF}) is shown in order to make clear that the dominant deformation mechanisms in austenitic steels are controlled by the stacking fault energy
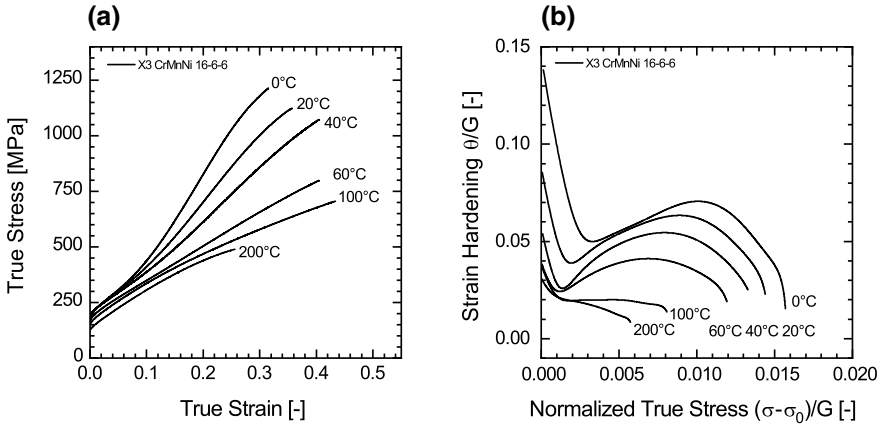

Fig. 11.39 Stress-strain curve (**a**) and strain hardening (**b**) of the X3CrMnNi16-6-6 TRIP/TWIP steel deformed at temperatures between 0 and 200 °C [4]

0.71($\cong \sqrt{2}/2$) for ε-martensite and twins, respectively, which is stored within the deformation bands because of the high SF density (see Sect. 11.2.3.1), contributes significantly to the overall dislocation based plasticity.

The alteration of deformation mechanisms with the temperature is also responsible for the change of the shape of the stress-strain curve and for the magnitude of the strain hardening (Fig. 11.39). The correlation between Figs. 11.38 and 11.39 confirms that the α'-martensite formation is a very effective hardening mechanism.

11.6 Conclusions

In this Chapter, the microstructure aspects of the deformation mechanisms in metastable austenitic steels were discussed. It was shown that the presence and form of the deformation bands play a crucial role in understanding the mechanical properties of the steels. It was demonstrated, that the deformation bands are composed of wide and tightly arranged stacking faults and, in some cases, of crossing deformation bands. The formation and widening of the stacking faults are the consequences of a low stacking fault energy of austenite, which facilitates the dissociation of perfect dislocations and the separation of partial dislocation under applied mechanical load. A high density of stacking faults within the deformation bands is recognized by diffraction methods (XRD, EBSD, SAED, FFT/HRTEM) either as an *hcp* stacking sequence, i.e., as ε-martensite, or as twinned austenite—depending on the SF density. A continuous transition between ε-martensite and twinned austenite is possible.

As the stacking fault energy of austenite depends strongly on its chemical composition and on temperature, already small variations in the kind and concentrations of the alloying elements and/or in the deformation temperature of the steel lead to serious changes in the dominant deformation mechanism. In many cases, perfect dislocations, isolated SFs, SF clusters, ε-martensite, twins and/or α'-martensite occur concurrently, but their fractions depend always on the stacking fault energy, and therefore on the steel composition, on the deformation temperature and on the deformation degree. Based on these results, the mechanical behavior of the TRIP/TWIP steels (mainly the ultimate tensile stress and the ultimate elongation) were related to the present microstructure defects and to their complex interplay. Formation of α'-martensite was found to contribute considerably to the strain hardening.

Finally, the potential of the in situ diffraction methods was illustrated. It was shown, how the stacking fault energy can be determined from the internal stresses measured during the deformation process and how the development of the deformation microstructure can be followed during an in situ deformation experiment.

References

1. H. Hasegawa, D.G. Pettifor, Phys. Rev. Lett. **50**, 130 (1983)
2. D. Bancroft, E.L. Peterson, S. Minshall, J. Appl. Phys. **27**, 291 (1956)
3. T. Takahashi, W. Bassett, Science **145**, 483 (1964)

4. S. Martin, S. Wolf, U. Martin, L. Krüger, D. Rafaja, Metall. Mater. Trans. **47**, 49 (2016)
5. W. Bleck, Werkstoffprüfung in Studium und Praxis, 15th edn. (Verlagsgruppe Mainz, 2011)
6. J.P. Hirth, J. Lothe, *Theory of Dislocations*, 2nd edn. (Krieger Publishing, Malabar, 1982)
7. P.C.J. Gallagher, Metall. Trans. **1**, 2429 (1970)
8. E.H. Lee, M.H. Yoo, T.S. Byun, J.D. Hunn, K. Farrell, L.K. Mansur, Acta Mater. **49**, 3277 (2001)
9. S.M. Copley, B.H. Kear, Acta Metall. **16**, 227 (1968)
10. T.S. Byun, Acta Mater. **51**, 3063 (2003)
11. M. Peach, J.S. Koehler, Phys. Rev. **80**, 436 (1950)
12. B.C. De Cooman, Y. Estrin, S.K. Kim, Acta Mater. **142**, 283 (2018)
13. A. Das, Metall. Mater. Trans. A **47**, 748 (2016)
14. F.C. Frank, W.R. Read, Phys. Rev. **79**, 722 (1950)
15. D. Hull, D.J. Bacon, *Introduction to Dislocations*, 5th edn. (Butterworth Heinemann, Oxford, 2011)
16. W.M. Lomer, Phil. Mag. **42**, 1327 (1951)
17. A.H. Cottrell, Phil. Mag. **43**, 645 (1952)
18. D. Borisova, V. Klemm, S. Martin, S. Wolf, D. Rafaja, Adv. Eng. Mater. **15**, 571 (2013)
19. N. Thompson, Proc. Phys. Soc. B **66**, 481 (1953)
20. S. Martin, C. Ullrich, D. Rafaja, Mater. Today: Proc. **2**, 643 (2015)
21. G.B. Olson, M. Cohen, Metall. Trans. A **7**, 1897 (1976)
22. D. Geissler, J. Freudenberger, A. Kauffmann, S. Martin, D. Rafaja, Phil. Mag. **94**, 2967 (2014)
23. P.J. Ferreira, P. Müllner, Acta Mater. **46**, 4479 (1998)
24. L. Vitos, J.-O. Nilsson, B. Johansson, Acta Mater. **54**, 3821 (2006)
25. A. Saeed-Akbari, J. Imlau, U. Prahl, W. Bleck, Metall. Mater. Trans. A **40**, 3076 (2009)
26. J. Nakano, P.J. Jacques, Calphad **34**, 167 (2010)
27. A.J.C. Wilson, Proc. R. Soc. London Ser. A **180**, 277 (1942)
28. M.S. Paterson, J. Appl. Phys. **23**, 805 (1952)
29. B.E. Warren, E.P. Warekois, Acta Metal. **3**, 473 (1955)
30. B.E. Warren, *X-Ray Diffraction*, 2nd edn. (Dover Inc., New York, 1990)
31. S. Martin, C. Ullrich, D. Šimek, U. Martin, D. Rafaja, J. Appl. Cryst. **44**, 779 (2011)
32. M.M.J. Treacy, J.M. Newsam, M.W. Deem, Proc. Roy. Soc. A **433**, 499 (1991)
33. L. Balogh, G. Ribárik, T. Ungár, J. Appl. Phys. **100**, 23512 (2006)
34. C. Ullrich, R. Eckner, L. Krüger, S. Martin, V. Klemm, D. Rafaja, Mater. Sci. Eng. A **649**, 390 (2016)
35. M.J. Whelan, P.B. Hirsch, Phil. Mag. **2**, 1303 (1957)
36. G. Thomas, W.L. Bell, H.M. Otte, Phys. Status Solidi A **12**, 353 (1965)
37. B. Cina, Acta Metall. **6**, 748 (1958)
38. C.W. Sinclair, R.G. Hoagland, Acta Mater. **70**, 4160 (2008)
39. H. Schumann, Krist. Tech. **9**, 1141 (1974)
40. A. Weidner, S. Martin, V. Klemm, U. Martin, H. Biermann, Scr. Mater. **64**, 513 (2011)
41. M. El-Tahawy, Y. Huang, T. Um, H. Choe, J.L. Lábár, T.G. Langdon, J. Gubicza, J. Mater. Res. Technol. **6**, 339 (2017)
42. C. E. Rodriguez Torres, F. H. Sánchez, A. González, F. Actis, R. Herreara, Metall. Mater. Trans. A **33**, 25 (2002)
43. K. Guy, E. Butler, D. Wes, J. de Phys. Colloques. **43**, 575 (1982)
44. L. Rémy, Acta Metall. **25**, 173 (1977)
45. R. Clendenen, H. Drickamer, J. Phys. Chem. Solids **25**, 865 (1964)
46. H.-K. Mao, W.A. Bassett, T. Takahashi, J. Appl. Phys. **38**, 272 (1967)
47. T. Takahashi, W.A. Bassett, M. Hokwang, J. Geophys. Res. B **73**, 4717 (1968)
48. P.M. Giles, M.H. Longenbach, A.R. Marder, J. Appl. Phys. **42**, 4290 (1971)
49. M. Friák, M. Šob, Phys. Rev. B **77**, 174117 (2008)
50. M. Friák, Steel Res. Int. **82**, 86 (2011)
51. N.A. Zarkevich, D.D. Johnson, Phys. Rev. B **91**, 174104 (2015)

52. S. Ackermann, S. Martin, M.R. Schwarz, C. Schimpf, D. Kulawinski, C. Lathe, S. Henkel, D. Rafaja, H. Biermann, A. Weidner, Metall. Mater. Trans. A **47**, 95 (2016)
53. H. Le Chatelier, Comptes Rendus **99**, 786 (1884)
54. M. Hillert, *Phase Equilibria, Phase Diagrams and Phase Transformations*, Chapter 6.9, 2nd edn. (Cambridge University Press, 2008)
55. J.R. Patel, M. Cohen, Acta Metall. **1**, 531 (1953)
56. L. Kaufman, M. Cohen, Prog. in Met. Phys. **7**, 165 (1958)
57. I. Tamura, Met. Sci. **16**, 245 (1982)
58. J.A. Venables, Phil. Mag. **7**, 35 (1962)
59. F. Lecroisey, A. Pineau, Metall. Trans. **3**, 387 (1972)
60. G.B. Olson, M. Cohen, J. Less Comm. Met. **28**, 107 (1972)
61. S. Martin, S. Wolf, S. Decker, L. Krüger, U. Martin, Steel Res. Int. **86**, 1187 (2015)
62. X.-S. Yang, S. Sun, T.-Y. Zhang, Acta Mater. **95**, 264 (2015)
63. Y. Tian, O.I. Gorbatov, A. Borgenstam, A.V. Ruban, P. Hedström, Metall. Mater. Trans. A **48**, 1 (2017)
64. A.J. Bogers, W.G. Burgers, Acta Metall. **12**, 255 (1964)
65. L. Bracke, L. Kestens, J. Penning, Scripta Mater. **57**, 385 (2007)
66. G. Kurdjumow, G. Sachs, Z. Phys. **64**, 325 (1930)
67. Z. Nishiyama, *Martensitic Transformation*, 1st edn. (Academic Press, New York, 1978)
68. G. Olson, M. Azrin, Metall. Mater. Trans. A **9**, 713 (1978)
69. J. Talonen, P. Aspegren, H. Hänninen, Mater. Sci. Technol. **20**, 1506 (2004)
70. L.S. Zevin, G. Kimmel, I. Mureinik, *Quantitative X-Ray Diffractometry* (Springer, New York, 1995)
71. H.M. Rietveld, J. Appl. Cryst. **2**, 65 (1969)
72. R.A. Young, *The Rietveld Method* (Oxford University Press, IUCr, 1993)
73. S. Allain, J.-P. Chateau, D. Dahmoun, O. Bouaziz, Mater. Sci. Eng. A **397–389**, 272 (2004)
74. O. Bouaziz, Scripta Mater. **66**, 982 (2012)
75. D.R. Steinmetz, T. Jäpel, B. Wietbrock, P. Eisenlohr, I. Gutierrez-Urrutia, A. Saeed-Akbari, T. Hickel, F. Roters, D. Raabe, Acta Mater. **61**, 494 (2013)
76. S. Allain, J.-P. Chateau, O. Bouaziz, Steel Res. Int. **79**, 299 (2002)
77. K. Renard, P.J. Jacques, Mater. Sci. Eng. A **542**, 8 (2012)
78. D. Barbier, N. Gey, S. Allain, N. Bozzolo, M. Humbert, Mater. Sci. Eng. A **540**, 212 (2012)
79. C. Schimpf, M. Motylenko, D. Rafaja, Mater. Char. **86**, 190 (2013)
80. M.A. Krivoglaz, *Theory of X-ray and Thermal Neutron Scattering by Real Crystals* (Plenum Press, New York, 1969)
81. M. Wilkens, Phys. Status Solidi A **2**, 359 (1970)
82. P. Klimanek, R. Kužel, J. Appl. Cryst. **21**, 59 (1988)
83. R. Kužel, P. Klimanek, J. Appl. Cryst. **21**, 363 (1988)
84. T. Ungár, G. Tichy, Phys. Status Solidi A **171**, 425 (1999)
85. T. Ungár, I. Dragomir, Á. Révész, A. Borbély, J. Appl. Cryst. **32**, 992 (1999)
86. A. Borbély, J. Dragomir-Cernatescu, G. Ribárik, T. Ungár, J. Appl. Cryst. **36**, 160 (2003)
87. I. Dragomir, T. Ungár, J. Appl. Cryst. **35**, 556 (2002)
88. N.C. Popa, J. Appl. Cryst. **31**, 176 (1998)
89. D.J.H. Cockayne, Phil. Mag. **20**, 1265 (1969)
90. C.C. Bampton, I.P. Jones, M.H. Loretto, Acta Metall. **26**, 39 (1978)
91. M.J. Mills, P. Stadelmann, Phil. Mag. A **60**, 355 (1989)
92. J. Lu, L. Hultman, E. Holmström, K.H. Antonsson, M. Grehk, W. Li, L. Vitos, A. Golpayegani, Acta Mater. **111**, 39 (2016)
93. M.J. Whelan, Proc. Roy. Soc. A **249**, 114 (1959)
94. A. Howie, P.R. Swann, Phil. Mag. **6**, 1215 (1961)
95. A. Ruff, L. Ives, Acta Metall. **15**, 189 (1967)
96. R.M. Latinision, A.W. Ruff, Metall. Trans. **2**, 505 (1971)
97. I.L. Dillamore, Phil. Mag. **9**, 517 (1964)
98. I.L. Dillamore, Metall. Trans. **1**, 2463 (1970)

99. R.P. Reed, R.E. Schramm, J. Appl. Phys. **45**, 4705 (1974)
100. R.E. Schramm, R.P. Reed, Metall. Trans. A **6**, 1345 (1975)
101. J. Talonen, H. Hänninen, Acta Mater. **55**, 6108 (2007)
102. T.-H. Lee, E. Shin, C.-S. Oh, H.-Y. Ha, S.-J. Kim, Acta Mater. **58**, 3173 (2010)
103. J.S. Jeong, W. Woo, K.H. Oh, S.K. Kwon, Y.M. Koo, Acta Mater. **60**, 2290 (2012)
104. D. Rafaja, C. Krbetschek, C. Ullrich, S. Martin, J. Appl. Cryst. **47**, 936 (2014)
105. D. Rafaja, C. Krbetschek, D. Borisova, G. Schreiber, V. Klemm, Thin Solid Films **530**, 103 (2013)
106. S. Allain, J.-P. Chateau, O. Bouaziz, S. Migot, N. Guelton, Mater. Sci. Eng. A **387–389**, 158 (2004)
107. S. Curtze, V.-T. Kuokkala, A. Oikari, J. Talonen, H. Hänninen, Acta Mater. **59**, 1068 (2011)
108. A. Abbasi, A. Dick, T. Hickel, J. Neugebauer, Acta Mater. **59**, 3041 (2011)
109. G.M. de Bellefon, J.C. van Duysen, K. Sridharan, J. Nucl. Mater. **492**, 227 (2017)
110. N. Chaudhary, A. Abu-Odeh, I. Karaman, R. Arróyave, J. Mater. Sci. **52**, 11048 (2017)
111. E. Kröner, Z. Phys. **151**, 504 (1958)
112. A. G. Every, A. K. McCurdy, Fe-Al-Nb-O, in *Springer Materials—The Landolt–Börnstein Database*ed. by D.F. Nelson (2011)
113. C. Ullrich, S. Martin, C. Schimpf, A. Stark, N. Schell, D. Rafaja, Adv. Eng. Mater. **21**, 1801101 (2019)
114. H. Van Swygenhoven, S. Van Petegem, Mater. Charact. **78**, 47 (2013)
115. L. Lutterotti, S. Matthies, H.-R. Wenk, A.S. Schultz, J.W. Richardson, J. Appl. Phys. **81**, 594 (1997)
116. L. Lutterotti, S. Matthies, H.-R. Wenk, IUCr Commission on Powder Diffraction Newsletter **21**, 14 (1999)
117. S. Matthies, G.W. Vinel, Phys. Status Solidi A **112**, K111 (1982)
118. M. Ferrari, L. Lutterotti, J. Appl. Phys. **76**, 7246 (1994)
119. A. Creuziger, C.A. Calhoun, W.A. Poling, T. Gnäupel-Herold, J. Appl. Cryst. **51**, 720 (2018)
120. S. Allain, J.-P. Chateau, O. Bouaziz, Mater. Sci. Eng. A **387–389**, 143 (2004)
121. T. Narutani, Mater. Trans. JIM **30**, 33 (1989)
122. M. Wilkens, Phys. Status Solidi A **104**, K1 (1987)
123. L. Rémy, Acta Metall. **26**, 443 (1978)
124. I. Gutierrez-Urrutia, D. Raabe, Acta Mater. **60**, 5791 (2012)
125. L. Rémy, Metall. Trans. A **12**, 387 (1981)
126. O. Bouaziz, S. Allain, C.P. Scott, P. Cugy, D. Barbier, Curr. Opin. Solid State Mater. Sci. **15**, 141 (2011)
127. S. Martin, O. Fabrichnaya, D. Rafaja, Mater. Lett. **159**, 484 (2015)
128. L. Rémy, A. Pineau, Mater. Sci. Eng. **28**, 99 (1977)